iScience

CellPress
OPEN ACCESS

Article

A Collagen10a1 mutation disrupts cell polarity in a medaka model for metaphyseal chondrodysplasia type Schmid

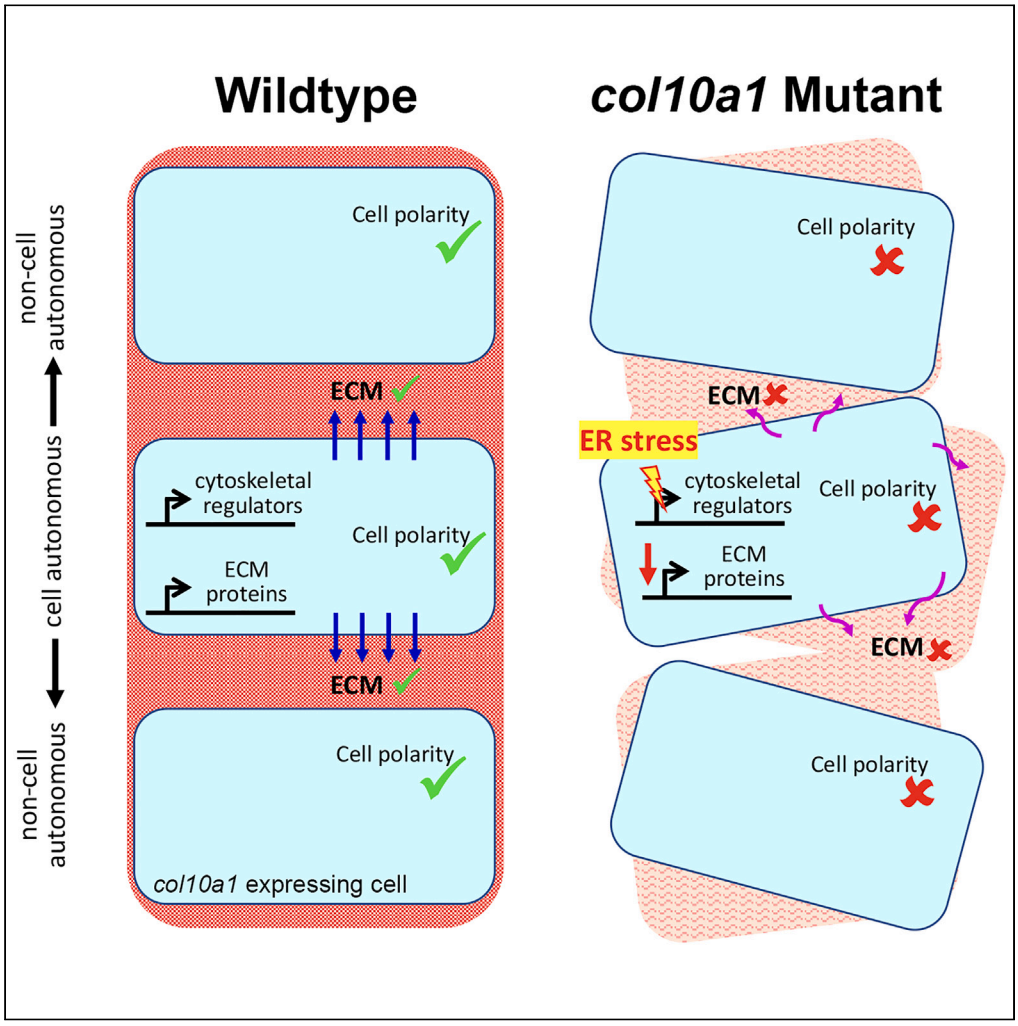

Wen Hui Tan, Martin Rücklin, Daria Larionova, ..., Federica Marone, Paul Matsudaira, Christoph Winkler

dbswcw@nus.edu.sg

Highlights

col10a1 medaka mutants recapitulate metaphyseal chondrodysplasia type Schmid (MCDS)

col10a1 medaka mutants exhibit elevated ER stress and skeletal deformities

Cell polarity is disrupted in chondrocytes and osteoblasts of *col10a1* mutants

Carbamazepine rescues polarity and structural defects in *col10a1* medaka mutants

Tan et al., iScience *27*, 109405
April 19, 2024
https://doi.org/10.1016/j.isci.2024.109405

iScience

CellPress
OPEN ACCESS

Article

A Collagen10a1 mutation disrupts cell polarity in a medaka model for metaphyseal chondrodysplasia type Schmid

Wen Hui Tan,[1] Martin Rücklin,[2] Daria Larionova,[3] Tran Bich Ngoc,[1] Bertie Joan van Heuven,[2] Federica Marone,[4] Paul Matsudaira,[1] and Christoph Winkler[1,5,*]

SUMMARY

Heterozygous mutations in *COL10A1* lead to metaphyseal chondrodysplasia type Schmid (MCDS), a skeletal disorder characterized by epiphyseal abnormalities. Prior analysis revealed impaired trimerization and intracellular retention of mutant collagen type X alpha 1 chains as cause for elevated endoplasmic reticulum (ER) stress. However, how ER stress translates into structural defects remained unclear. We generated a medaka (*Oryzias latipes*) MCDS model harboring a 5 base pair deletion in *col10a1*, which led to a frameshift and disruption of 11 amino acids in the conserved trimerization domain. *col10a1*$^{\Delta 633a}$ heterozygotes recapitulated key features of MCDS and revealed early cell polarity defects as cause for dysregulated matrix secretion and deformed skeletal structures. Carbamazepine, an ER stress-reducing drug, rescued this polarity impairment and alleviated skeletal defects in *col10a1*$^{\Delta 633a}$ heterozygotes. Our data imply cell polarity dysregulation as a potential contributor to MCDS and suggest the *col10a1*$^{\Delta 633a}$ medaka mutant as an attractive MCDS animal model for drug screening.

INTRODUCTION

Metaphyseal chondrodysplasia type Schmid (MCDS; OMIM 156500) is a rare autosomal dominant skeletal disorder characterized by irregular growth plates, bowed legs, hip deformities, and short stature.[1,2] In MCDS, missense mutations or mutations resulting in a premature stop codon occur in the trimerization domain of the *COL10A1* gene, leading to the production of a mutant collagen type X protein with disrupted trimer assembly and defective extracellular secretion.[1,2] At present, no drug has been approved for the treatment of MCDS. However, carbamazepine (CBZ), an anti-epileptic drug, was shown to attenuate MCDS disease severity in mouse models[3,4] and is currently tested in a clinical trial for MCDS treatment (https://mcds-therapy.eu/). Collagen type X is a non-fibrillar short-chain collagen comprising homotrimers of α1 chains. In mammals, the *COL10A1* gene is expressed in hypertrophic chondrocytes during endochondral ossification, a process of bone formation involving a cartilage intermediate that is progressively replaced by calcified bone.[5–8] Earlier *in vitro* studies showed that collagen type X assembles into supramolecular hexagonal lattice structures in the extracellular matrix (ECM) and forms covalent cross-links with other ECM components such as collagens type II and type IX.[9,10] However, the precise role of collagen type X in endochondral ossification is not clear as results in null mutant mice are conflicting.[11,12]

Studies using MCDS patient samples and transgenic and knockin mouse models, as well as *in vitro* models, showed that a dominant mechanism contributes to the majority of MCDS pathologies. These studies indicated that in MCDS mutant collagen type X is intracellularly retained due to defective trimer assembly.[13–15] Intracellular accumulation of mutant protein subsequently leads to increased endoplasmic reticulum (ER) stress, activating the unfolded protein response (UPR).[15,16] Importantly, experimental induction of ER stress in hypertrophic chondrocytes of mice expressing normal collagen type X was sufficient to cause growth plate abnormalities, demonstrating a key role of ER stress in MCDS pathology.[17] To assess molecular changes downstream of ER stress, transcriptome analyses of deformed growth plate cartilage in homozygous MCDS mice were performed. These analyses revealed enrichment of dysregulated genes in pathways including protein folding and degradation, ECM-receptor interactions, and metabolism-related pathways.[18,19] In addition, retained expression of proliferative markers in the hypertrophic growth plate suggested developmental arrest of hypertrophic chondrocytes.[18] How these changes contribute to impaired growth plate modeling and skeletal deformities in MCDS, however, remained unclear. All previously identified MCDS patients carry a heterozygous *COL10A1* mutation, and a study conducted by Zhang et al.[20] suggested that a homozygous *COL10A1* p.Asn617Lys mutation could be embryonic lethal.[1,20] In striking contrast to the human situation, heterozygous mice carrying a

[1]Department of Biological Sciences and Centre for Bioimaging Sciences, National University of Singapore, Singapore 117543, Singapore
[2]Naturalis Biodiversity Center, Postbus 9517, 2300 RA Leiden, the Netherlands
[3]Department of Biology, Research Group Evolutionary Developmental Biology, Ghent University, Ghent, Belgium
[4]Swiss Light Source, Paul Scherrer Institut, CH-5232 Villigen, Switzerland
[5]Lead contact
*Correspondence: dbswcw@nus.edu.sg
https://doi.org/10.1016/j.isci.2024.109405

p.Asn617Lys mutation in collagen type X in an SV129/C57Bl6 mixed background showed only subtle MCDS phenotypes,[17] while homozygosity of the mutant allele resulted in a phenotype more similar to MCDS patients.[17]

To uncover how ER stress leads to skeletal deformities in MCDS, we took advantage of the teleost medaka (*Oryzias latipes*) that together with zebrafish has been increasingly used as model to study human bone and cartilage disorders.[21–23] Many important aspects of osteochondral development and bone mineral composition, as well as ER stress pathways that have been implicated in several chondrodysplasias,[24] are conserved in teleost fish.[25–27] Currently, there is no teleost model for MCDS, but two *col10a1* orthologs, *col10a1a* (previously known as *col10a1*; referred to as *col10a1* in this study) and *col10a1b*, have been annotated in medaka and zebrafish genomes. In medaka, *col10a1* is expressed in chondrocytes and osteoblast progenitors during early skeletal development.[28,29]

Here, we characterized the medaka *col10a1*$^{\Delta 633a}$ mutant, which harbors a mutation that corresponds to MCDS mutations identified in patients.[20,30,31] We show that *col10a1*$^{\Delta 633a}$ heterozygotes exhibited key MCDS features such as impaired endochondral bone formation and short stature. In addition, *col10a1*$^{\Delta 633a}$ mutant chondrocytes lost their organized stacking in cartilage suggesting a possible loss of cell polarity. Consistent with this, mutant *col10a1* cells exhibited impaired localization of polarized microtubule-organizing centers (MTOCs) and Golgi apparatus, a randomization of nuclear division axes, and dysregulation of cytoskeleton modeling factors, which are important regulators of cell polarity. We found that extracellular secretion of mutant medaka collagen type X was disrupted, and ER stress markers were elevated. Finally, we show that CBZ treatment alleviated ER stress in heterozygous *col10a1*$^{\Delta 633a}$ mutants and rescued cell polarity and skeletal defects. Together, our data implicate loss of cell polarity as a potential contributor to MCDS and validate the *col10a1*$^{\Delta 633a}$ medaka mutant as a suitable MCDS model for drug testing.

RESULTS

Heterozygous *col10a1*$^{\Delta 633a}$ medaka mutants have shortened ceratohyal bones and body stature

Two medaka *col10a1* orthologs, *col10a1a* (previously known as and referred to in this study as *col10a1*) and *col10a1b*, are listed in Ensembl (ENSORLG00000013436; ENSORLG00000027315). Both orthologs encode proteins with similar predicted sizes and domains and an overall amino acid (aa) similarity of 78% (Figure 1A). Alignment of the trimerization domains of both medaka proteins to human collagen type X also revealed a high level of aa similarity (Col10a1, 78%; Col10a1b, 79%; Figure 1A). In this study, we used CRISPR-Cas9 to mutate the region of *col10a1* that encodes the trimerization domain of collagen type X, generating a *col10a1*$^{\Delta 633a}$ medaka mutant that harbors a 5 base pair (bp) deletion (Figures 1B–1D). This deletion is predicted to result in a frameshift at aa position 633, disrupting the last 11 aa and elongating the protein by one aa (Figure 1D; underlined in yellow). This alteration affects a region where two *COL10A1* mutations were previously reported in MCDS patients: a p.Ser671Pro missense mutation[20,31] and a p.Val677TrpfsTer10 frameshift mutation[30] (Figure 1D). Sequencing analysis confirmed that the guide RNA (gRNA) used for generating *col10a1*$^{\Delta 633a}$ mutants did not target *col10a1b* (n = 3 heterozygous *col10a1*$^{\Delta 633a}$ mutants sequenced; Figure S1).

To examine mutant viability, *col10a1*$^{\Delta 633a}$ heterozygotes were incrossed and F_1 progeny were genotyped at 12- and 18-day post fertilization (dpf), as well as 1 and >3 months post fertilization (mpf) (Figure 1E). At 12 dpf, the expected 1:2:1 Mendelian ratio of wild-type (WT) and mutant (m) alleles was observed (26.6% WT/WT, 48.9% WT/m, 24.5% m/m; n = 94 fish). At 18 dpf, however, the number of surviving homozygous (m/m) mutants was reduced (29.8% WT/WT, 63.2% WT/m, 7.0% m/m; n = 57 fish), and, at 1 mpf or later, no more m/m mutants could be identified (n = 119 fish; Figure 1E). On the other hand, survival of heterozygous (WT/m) mutants was in line with the expected Mendelian ratio up to 1 mpf but declined beyond 3 mpf (Figure 1E). At 3 mpf, WT/m mutants had a shorter body length (1.98 $\pm$ 0.0425 cm) compared to WT/WT siblings (2.38 $\pm$ 0.0488 cm; Figure 1F). Quantification of the number and length of vertebral bodies revealed similar numbers in WT/m mutants and WT/WT siblings but shorter vertebral body (VB) length in mutants (Figure S2). This suggested normal vertebral segmentation but impaired longitudinal bone growth in mutant vertebral bodies over time. Consistent with this, growth was also impaired in the ceratohyal, an endochondral bone where *col10a1* is expressed in hypertrophic chondrocytes of the growth plate (Figures 1F and S3). In WT/m mutants, the ceratohyal was shorter (1.37 $\pm$ 0.0363 mm) when compared to WT/WT siblings (1.53 $\pm$ 0.0355 mm; Figure 1F). Hence, this suggests impaired endochondral ossification in medaka *col10a1*$^{\Delta 633a}$ mutants, reminiscent of the phenotypes reported in human MCDS patients.

col10a1$^{\Delta 633a}$ medaka mutants have delayed, irregular, and ectopic bone formation

Endogenous *col10a1* expression in medaka is first seen in the cranial skeleton at 4 dpf and in the vertebral column at 6 dpf.[28] To test whether the *col10a1*$^{\Delta 633a}$ mutation affects early osteogenesis, we examined osteoblast formation and bone development in *col10a1*$^{\Delta 633a}$ mutants by RNA *in situ* hybridization using osteoblast differentiation markers *runx2*, *col10a1*, and *osx* (Figure S4). In the cranium at 4 dpf, expression of the mesenchymal progenitor marker *runx2* was similar in WT/WT controls, as well as WT/m and m/m mutants (Figures S4A–S4A″). At 6 dpf, however, expression of *col10a1* (marking osteoblast progenitors;[28] Figures S4B–S4B″) and *osx* (labeling premature osteoblasts;[32] Figures S4C–S4C″) was reduced in WT/m and m/m mutants, with a more severe reduction in m/m mutants (Figures S4B″ and S5C″). This suggested a mild and severe disruption of osteoblast differentiation in *col10a1*$^{\Delta 633a}$ WT/m and m/m mutants, respectively. Consequently, this resulted in delayed mineralization and deformed cranial skeletal structures, as well as absence of mineralized vertebral arches in *col10a1*$^{\Delta 633a}$ m/m mutants at 12 and 18 dpf (Figure S5). In WT/m mutants, on the other hand, cranial skeletal structures were mineralized, however, to a lesser extent than in WT/WT siblings (Figure S5). Cleithrum, operculum, and branchiostegal rays appeared irregular, and the edges of vertebral bodies were hypermineralized in WT/m mutants but not in WT/WT siblings at 18 dpf (Figure S5B).

At adult stages, micro-computed tomography (micro-CT), synchrotron X-ray imaging, and alizarin red staining revealed enhanced and ectopic bone formation in WT/m mutants along vertebral arches (Figures 2A, 2A′, 2B, 2B′, S6A, S6A′, S6B, and S6B′; yellow arrows) and in

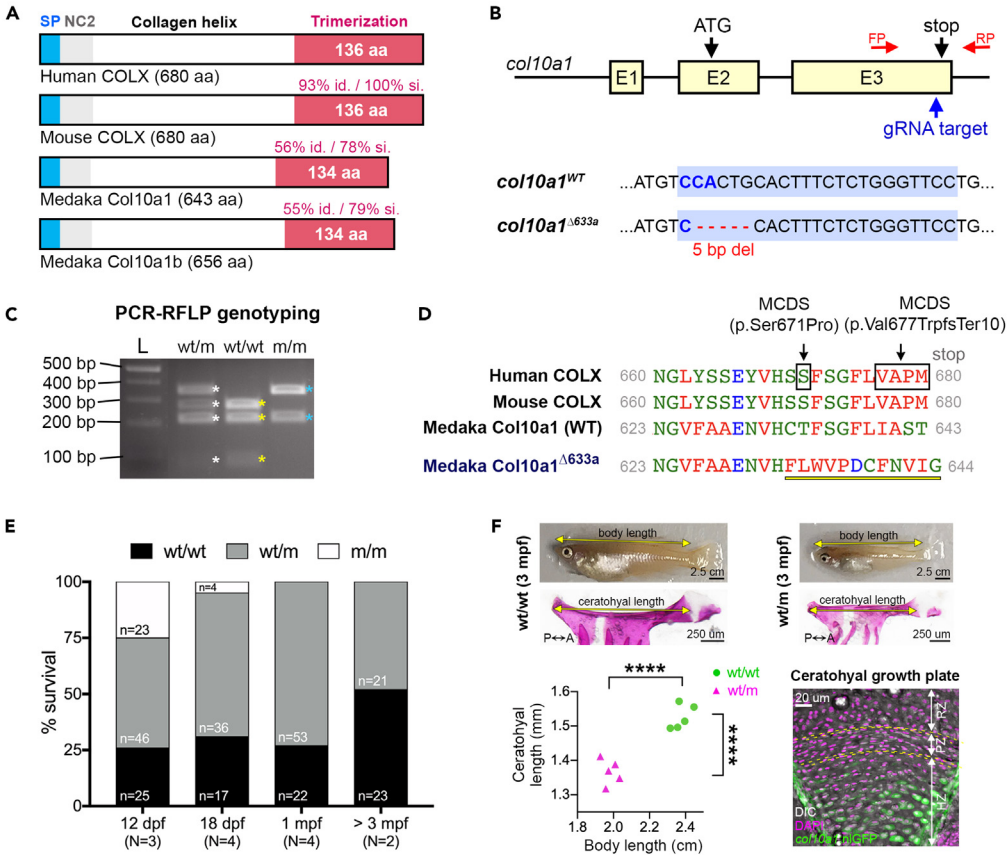

Figure 1. Generation of *col10a1*$^{\Delta 633a}$ medaka mutants by CRISPR-Cas9

(A) Schematic comparison of human Collagen type X alpha 1 (ColX), mouse ColX, medaka Col10a1, and medaka Col10a1b. Percentage identity (id.) and similarity (si.) are in reference to human ColX and obtained from Clustal Omega Multiple Sequence Alignment. aa, amino acid; SP, signal peptide; NC2, non-collagenous 2 domain.

(B) CRISPR/Cas9 guide RNA (gRNA) design for the generation of *col10a1*$^{\Delta 633a}$ medaka mutants. A gRNA targeting *col10a1* at exon 3 (E3) was used to generate mutants that harbor a 5 base pair (bp) deletion at the gRNA PAM sequence (CCA; highlighted in blue).

(C) Genotyping of *col10a1*$^{\Delta 633a}$ medaka mutants performed by PCR-RFLP using the primer pair annotated in B (FP, RP; red arrows) and *BtsI* for restriction digest. Three DNA products of sizes 287 bp, 225 bp, and 84 bp were observed for wild-type siblings (WT/WT; yellow asterisks), two bands of 371 bp and 225 bp were observed for homozygous (m/m; blue asterisks), and four bands of 371 bp, 287 bp, 225 bp, and 84 bp for heterozygous mutants (WT/m; white asterisks).

(D) Clustal Omega amino acid sequence alignment of the last 21 aa of human ColX, mouse ColX, medaka wild-type (WT) Col10a1 and medaka Col10a1$^{\Delta 633a}$. The mutated region in Col10a1$^{\Delta 633a}$ (underlined in yellow) corresponds to p.Ser671Pro and p.Val677TrpfsTer10 mutations identified in MCDS patients. Physicochemical properties of amino acid residues: red, hydrophobic; blue, acidic; green, basic/polar/sulfhydryl/G.

(E) Survival analysis of F_1 progenies from incrosses of heterozygous *col10a1*$^{\Delta 633a}$ medaka mutants at four different time points (12 days post fertilization, dpf, 18 dpf, 1 month post fertilization, mpf and >3 mpf). N, number of independent clutches. n, number of fish.

(F) Body and ceratohyal length measurements of WT/WT siblings and *col10a1*$^{\Delta 633a}$ WT/m mutants at 3 mpf. Ceratohyals were stained using alizarin red. Yellow arrows indicate the length measured. A, anterior; P, posterior. ****p < 0.0001, Student's two-tailed t test. n = 5 fish. Confocal image at the bottom right shows a 20 μm cryosection of a *col10a1*$^{w/w}$ medaka ceratohyal growth plate (2 mpf). *col10a1*:nlGFP expression was detected in the hypertrophic zone (HZ). DAPI-stained nuclei, yellow dotted lines demarcate resting zone (RZ), proliferative zone (PZ), and HZ of growth plate. Scale bars are indicated in the images.

skeletal structures in the head region such as the parasphenoid (Figures 2A″ and 2B″; white arrowheads), pharyngeal jaw structures (Figures 2A″ and 2B″; cyan arrowheads), and gill filaments (Figures 2A″, 2A‴, 2B″, and 2B‴; yellow arrowheads). In line with this, expression of *alkaline phosphatase* (*alpl*), encoding an enzyme which promotes mineralization,[33] was upregulated in dissected head tissues including the branchial arches, pharyngeal jaw, and gills of WT/m mutants at 5 mpf (Figure S6C). Furthermore, the regular mineralization pattern in scales was lost (Figures 2A⁗, 2B⁗, S6A‴, and S6B‴). Previous studies have shown that *col10a1* is also expressed in medaka teeth[34] and bony fin rays.[35] Accordingly, structural irregularities were also observed in the mutant caudal fin, where the fin rays were crooked and had more fractures compared to WT/WT siblings (Figures 2C and 2D; green arrows), and at the mutant oral region, where teeth appeared more sparse and less developed compared to WT/WT siblings (Figures 2E and 2F; white arrows). Together, this suggested that impaired differentiation and function of *col10a1* cells led to irregular bone mineralization in *col10a1*$^{\Delta 633a}$ heterozygotes.

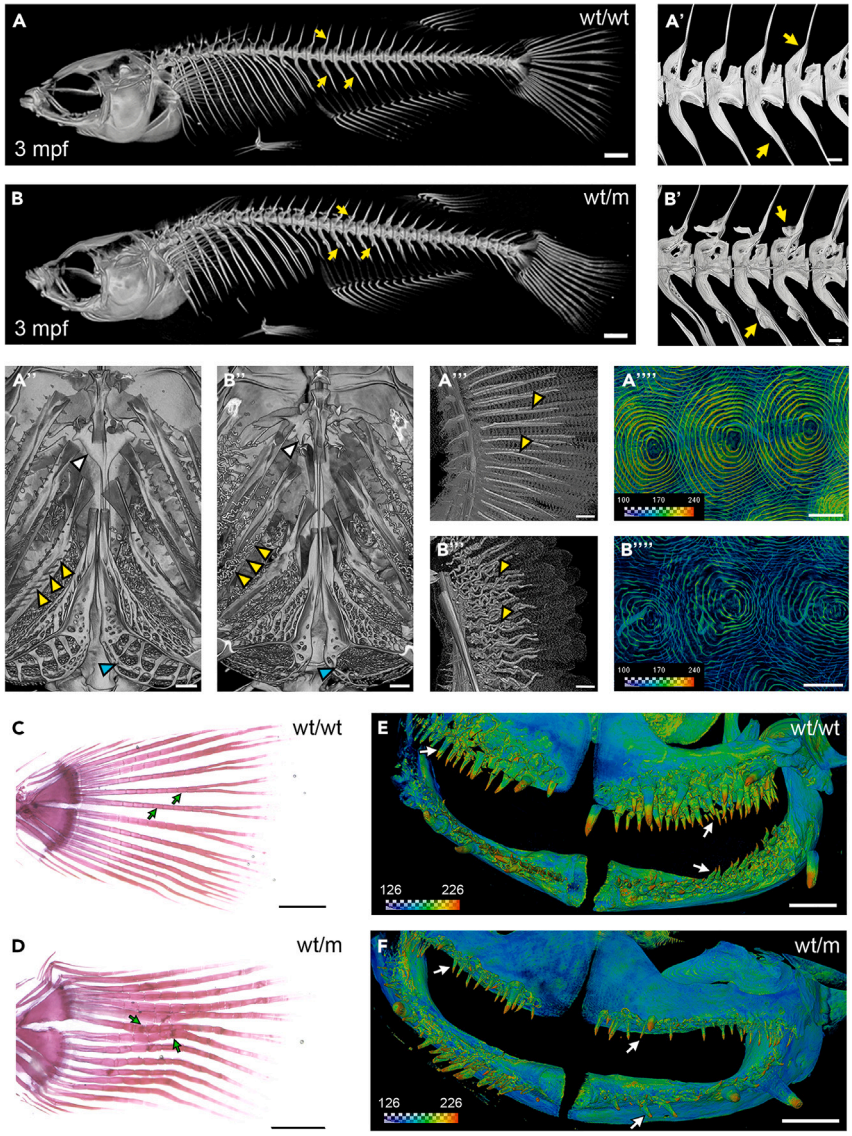

Figure 2. Ectopic bone formation in *col10a1*$^{\Delta 633a}$ WT/m adults

(A–B‴′) Micro-CT (A–A″, B–B″) and synchrotron X-ray (A‴, A‴′, B‴, B‴′) tomographic images of WT sibling (A–A‴′) and heterozygous *col10a1*$^{\Delta 633a}$ medaka mutant (B–B‴′) at 3 mpf. Fish of approximately same body length were chosen for analysis (for distribution of wild-type and mutant body lengths, see Figure 1F). Overview (A, B) as well as magnified views of the vertebral column (A′, B′), cranial region (A″, B″), gills (A‴, B‴) and scales (A‴′, B‴′). Images in (A–A‴) and (B–B‴) are in greyscale while images in (A‴′) and (B‴′) are shown in a color with the color scale related to tissue density (red reflects high and blue low density). Yellow arrows, vertebral arches. White arrowheads, parasphenoid. Yellow arrowheads, gill filaments. Cyan arrowheads, pharyngeal jaw.

(C and D) Alizarin red-stained caudal fin of a WT sibling (C) and heterozygous *col10a1*$^{\Delta 633a}$ medaka mutant (D) at 2.5 mpf. Green arrows indicate fin rays.

(E and F) Synchrotron X-ray tomographic images of a WT sibling (E) and heterozygous *col10a1*$^{\Delta 633a}$ medaka mutant (F) at 3 mpf showing sparse and less developed teeth in the mutant. Scale bars: (A, B, C, D) 1000 μm, (A′, A″, A‴′, B′, B″, B‴′, E, F) 200 μm, (A‴, B‴) 100 μm.

Nondirectional bone matrix secretion and aberrant Golgi localization in mutant *col10a1* osteoblast progenitors

In medaka, other than in mammals, vertebral bodies form by intramembranous ossification, i.e., in the absence of a cartilage scaffold.[27] Osteoblasts at the vertebral bodies are always positioned on top of directionally secreted bone matrix but do not get embedded in matrix to become osteocytes, in contrast to, e.g., osteocytic zebrafish.[36,37] To examine the cellular basis of irregular bone formation in *col10a1*$^{\Delta 633a}$ WT/m mutants, the behavior of osteoblast progenitors was assessed in *col10a1*:nlGFP transgenic larvae[28] stained with alizarin complexone (ALC; Figures 3A–3B‴). In WT/WT siblings at 18 dpf, most *col10a1*:nlGFP osteoblast progenitor cells lined the edges of vertebral centra and were positioned outside the mineralized matrix (Figures 3A–3A‴; yellow asterisks). In contrast, the edges of vertebral bodies in WT/m mutants were hypermineralized (Figure 3B′; yellow arrows; Figure S5B; orange arrowheads), with a significant overlap of *col10a1* cells with the

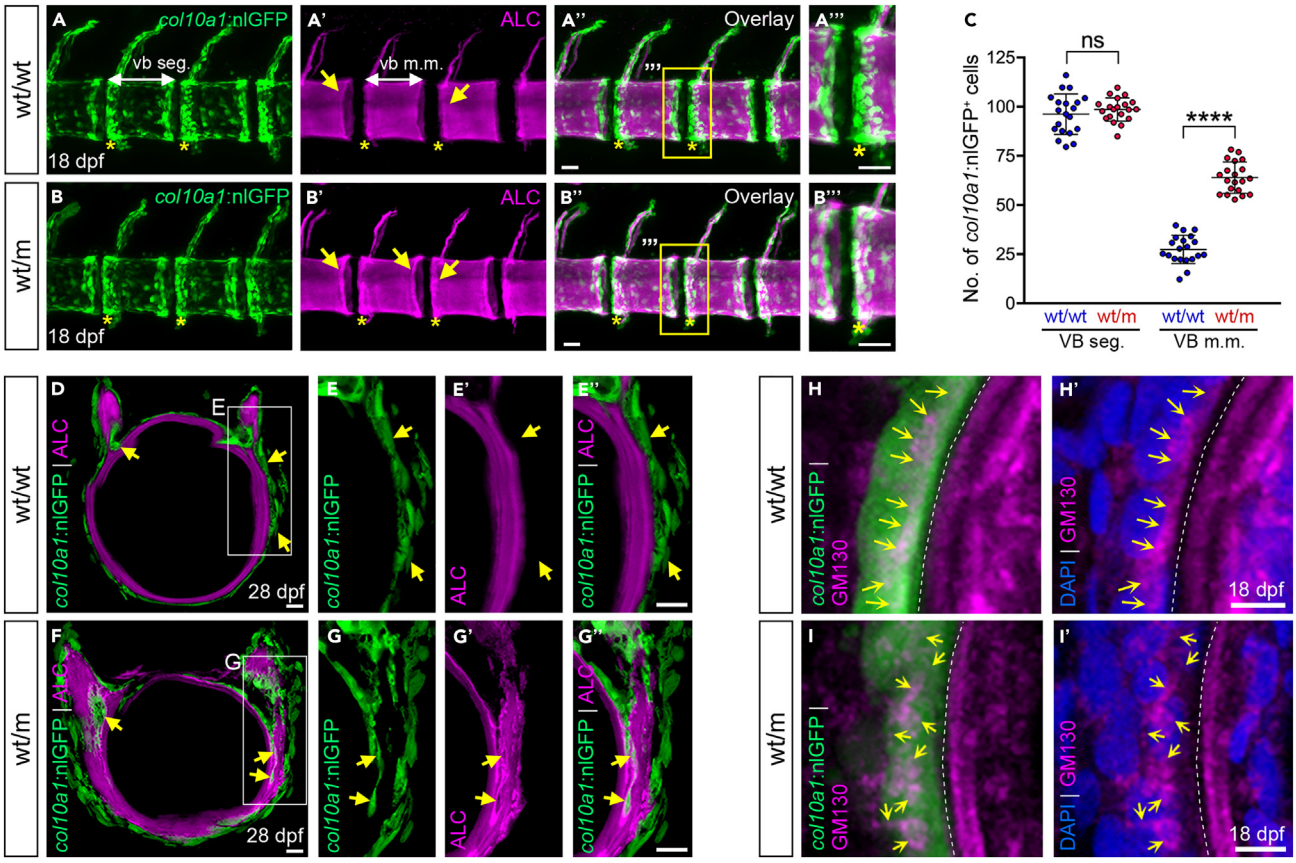

Figure 3. *col10a1*:nlGFP-expressing osteoblast progenitors are trapped within irregular bone matrix in WT/m *col10a1*$^{\Delta 633a}$ medaka mutants

(A–B‴) Confocal 3D images showing lateral views of *col10a1*:nlGFP-expressing osteoblast progenitors and alizarin complexone (ALC)-stained mineralized matrix in the vertebral column of WT/WT controls (A–A‴) and *col10a1*$^{\Delta 633a}$ WT/m mutants (B–B‴). Boxes in (A″)and (B″) indicate magnified views as shown in (A‴)and (B‴), respectively. Compared to WT/WT siblings, edges of vertebral bodies in WT/m mutants were hypermineralized (A′, B′, arrows) and had increased overlap with *col10a1*:nlGFP-expressing cells (A′–A‴, B′–B‴, asterisks).

(C) Quantification of total numbers of *col10a1*:nlGFP-expressing cells per vertebral body segment (VB seg.) and those that overlap with the VB mineralized matrix (VB m. m.) as shown in A–B‴. n = 5 fish, 4 vertebral bodies per fish. Error bars indicate mean ± s.d., ****p < 0.0001, ns, not significant, Student's two-tailed t test.

(D–G″) Confocal 2D images showing transverse views of *col10a1*:nlGFP-expressing osteoblast progenitors and ALC-stained mineralized matrix in the vertebral column of WT/WT controls (D–E″) and WT/m mutants (F–G″). Boxes in (D) and (F) indicate magnified views as shown in (E)–(E″) and (G)–(G″), respectively. Yellow arrows in (D)–(E″) indicate *col10a1*:nlGFP-expressing cells that line the surface of mineralized matrix in WT/WT controls. Yellow arrows in (F)–(G″) indicate *col10a1*:nlGFP-expressing cells trapped within the irregularly formed matrix in WT/m mutants.

(H–I′) Confocal 3D images showing transverse sections of the vertebral column in a *col10a1*:nlGFP-expressing WT/WT sibling (H, H′) and WT/m mutant (I, I′) at 18 dpf. Cryosections were stained with GM130 and DAPI for visualization of Golgi apparatus and nuclei, respectively. Yellow arrows indicate GM130-stained Golgi in *col10a1*:nlGFP-expressing cells. Dotted lines indicate mineralized matrix of the vertebral column. Scale bars: (A–B‴) 25 μm, (D–G″) 10 μm, (H–I′) 5 μm.

mineralized matrix (Figure 3B–3B‴; yellow asterisks). Quantification showed no difference in total numbers of *col10a1*:nlGFP cells per VB segment (vb seg.; indicated in Figure 3A) in WT/WT and WT/m siblings (Figure 3C; n = 20 VBs, 5 fish). However, the number of cells embedded within mineralized matrix (VB m.m.; indicated in Figure 3A′) was higher in WT/m than in WT/WT siblings (Figure 3C; n = 20 VBs, 5 fish).

Transverse cryosections of the vertebral column at the edge of a VB (yellow arrows in Figures 3A′ and 3B′) showed that, while all *col10a1*:nlGFP-expressing cells were located on top of the ALC-stained mineralized matrix in WT/WT controls as expected (Figures 3D–3E″; yellow arrows; n = 5 fish), several *col10a1*:nlGFP-expressing cells were trapped within the mineralized matrix in WT/m mutants (Figures 3F–3G″; yellow arrows; n = 5 fish). Importantly, compared to the uniformly mineralized bone surface in WT/WT controls (Figures 3D and 3E′), the bone surface in WT/m mutants was unevenly mineralized (Figures 3F and 3G′). In addition, GM130 immunostaining on transverse cryosections of the vertebral column showed that in WT/WT *col10a1*:nlGFP osteoblast progenitors, the Golgi apparatus was consistently positioned along one side of cells proximal to the notochord (Figures 3H and 3H′; yellow arrows indicate Golgi apparatus, white dotted lines indicate notochord edge). In contrast, this regular positioning was lost in WT/m progenitors, where GM130-stained Golgi were randomly distributed both distal and proximal to the notochord (Figures 3I and 3I′; yellow arrows indicate Golgi, dotted lines mark notochord edge). Together, these observations strongly suggest that in WT/WT siblings, *col10a1*:nlGFP-expressing cells secrete bone matrix in a

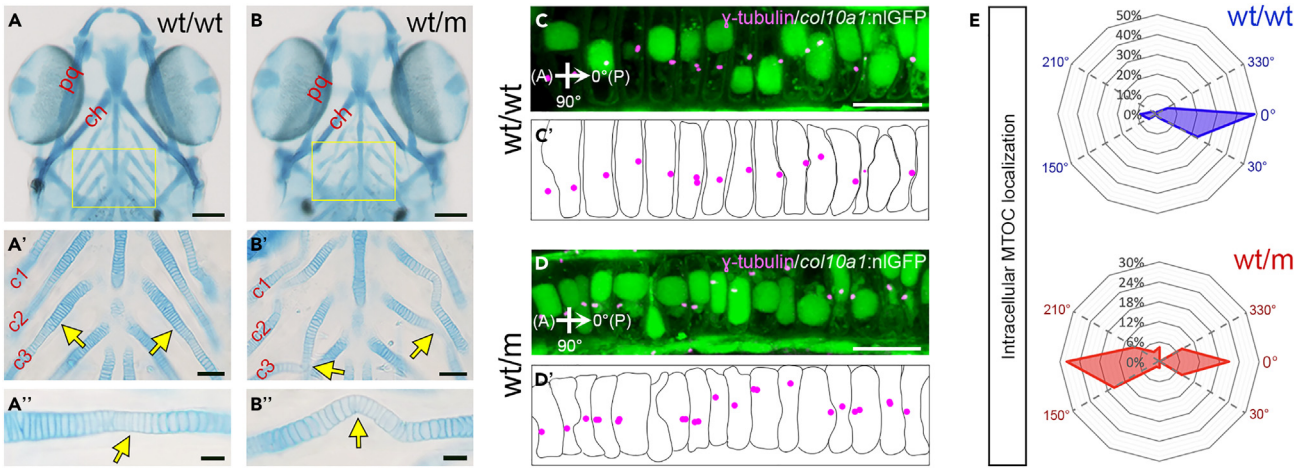

Figure 4. Impaired *col10a1* chondrocyte polarity and disorganization of cartilage structures in *col10a1*$^{\Delta 633a}$ WT/m mutants

(A–B″) Alcian blue staining of head region in a WT/WT sibling (A–A″) and *col10a1*$^{\Delta 633a}$ WT/m mutant (B–B″) at 12 dpf. Yellow boxes in (A) and (B) indicate magnified views as shown in A′ and B′, respectively. Yellow arrows indicate chondrocytes in the ceratobranchials. A″ and B″ are magnified views showing chondrocyte stacking in one ceratobranchial of WT/WT sibling and WT/m mutant, respectively. pq, palatoquadrate; ch, ceratohyal; c1-c3, ceratobranchials 1-3. (C–D′) Ceratobranchial chondrocytes in WT/WT sibling (C, C′) and *col10a1*$^{\Delta 633a}$ WT/m mutant (D, D′) at 16 dpf, showing *col10a1*:nlGFP expression and γ-tubulin-stained microtubule-organizing centers (MTOCs; magenta). (C′) and (D′) show schematic illustrations of γ-tubulin-stained MTOCs in (C) and (D), respectively. A, anterior; P, posterior.

(E) Graphical representation of the location of γ-tubulin-stained MTOCs in chondrocytes as shown in (C)–(D′). $n_{wt/wt}$ = 82 cells, 5 fish; $n_{wt/m}$ = 115 cells, 5 fish. Scale bars: (A, B) 100 μm, (A′, B′) 25 μm, (A″, B″, C, D) 5 μm.

unidirectional manner and become positioned on top of the mineralized matrix. In contrast, in WT/m mutants, non-polarized matrix secretion leads to irregular mineralization and trapping of *col10a1*:nlGFP cells within the mineralized matrix.

Impaired chondrocyte polarity and deformed cartilage in heterozygous *col10a1*$^{\Delta 633a}$ medaka mutants

Besides osteoblast progenitors, medaka *col10a1* is also expressed in chondrocytes of developing cartilaginous structures such as ceratobranchials and palatoquadrate.[29] We thus examined cartilage formation in *col10a1*$^{\Delta 633a}$ WT/m medaka mutants. At 12 dpf, Alcian blue staining showed overall normal formation of cartilaginous structures in WT/m mutants when compared to WT/WT except in the ceratobranchials, where WT/m mutants exhibited impaired stacking of chondrocytes as opposed to the regular columnar arrangement in WT/WT siblings (Figures 4A–4B″; yellow arrows; n = 5 fish). In zebrafish, cell polarity plays an important role in proper chondrocyte stacking.[38] To test if aberrant chondrocyte stacking in *col10a1*$^{\Delta 633a}$ WT/m medaka mutants was due to a loss of cell polarity, the position of γ-tubulin-positive microtubule-organizing centers (MTOCs) was determined in ceratobranchials at 16 dpf (Figures 4C–4E). Compared to WT/WT chondrocytes, where a majority of MTOCs was found within a 330°–30° cell domain (n = 64/82 cells, 78%, 5 fish; Figures 4C, 4C′, and 4E), MTOCs in WT/m chondrocytes were often positioned at opposing ends of cells in the 150°–210° domain (n = 60/115, 52%, n = 5 fish), in addition to the 330°–30° cell domain (n = 42/115, 37%, 5 fish; Figures 4D, 4D′, and 4E) indicating impaired cell polarity. Consistent with this, confocal imaging of *col10a1*:nlGFP chondrocytes in the ceratohyal growth plate also revealed rounder nuclear morphology and atypical longitudinal nuclear axes in mutant cells, suggesting disrupted cell polarity (Figure S7; n = 3 fish). Furthermore, X-ray microtomography and Alcian blue staining of adult WT/m mutants also showed that cartilaginous gill filaments, which extend from ceratobranchials, were strongly distorted (Figures 2A‴, 2B‴, yellow arrowheads; Figures S8A–S8B′; n = 5 fish). Confocal imaging of *col10a1*:nlGFP expression in gill filaments at 3 mpf confirmed impaired chondrocyte stacking (Figures S8C–S8F′). Finally, correlative light-electron microscopy (CLEM) analysis indicated that chondrocytes in gill filaments that are known to continue to divide for self-renewal at post-embryonic stages[39] also had altered nuclear division axes in WT/m mutants when compared to WT/WT (Figures S8G–S8I). At 3 mpf, a majority of WT/WT control chondrocytes had a nuclear division angle between 60° and 90° with respect to the longitudinal cell axis (n = 18/30 cells, 60%, 3 fish; Figures S8H and S8I). In contrast, most mutant chondrocytes had a division angle between 20° and 50° (n = 12/19 cells, 63%, 3 fish; Figures S8H and S8I). This reduction in perpendicularity may account for the irregular columnar stacking of chondrocytes observed in *col10a1* mutant cartilage structures.

Mutant medaka collagen type X protein is retained intracellularly and heterozygous *col10a1*$^{\Delta 633a}$ mutants have elevated ER stress

In MCDS, mutations in the trimerization domain of collagen type X disrupt its post-translational processing, resulting in intracellular retention of mutant protein.[15,17] To test if the 5 bp deletion in *col10a1*$^{\Delta 633a}$ mutants also leads to defective protein secretion, mRNAs encoding medaka WT Col10a1 or mutant Col10a1$^{\Delta 633a}$, both N-terminally tagged with a Myc-epitope, were injected into a single cell of four-cell stage medaka

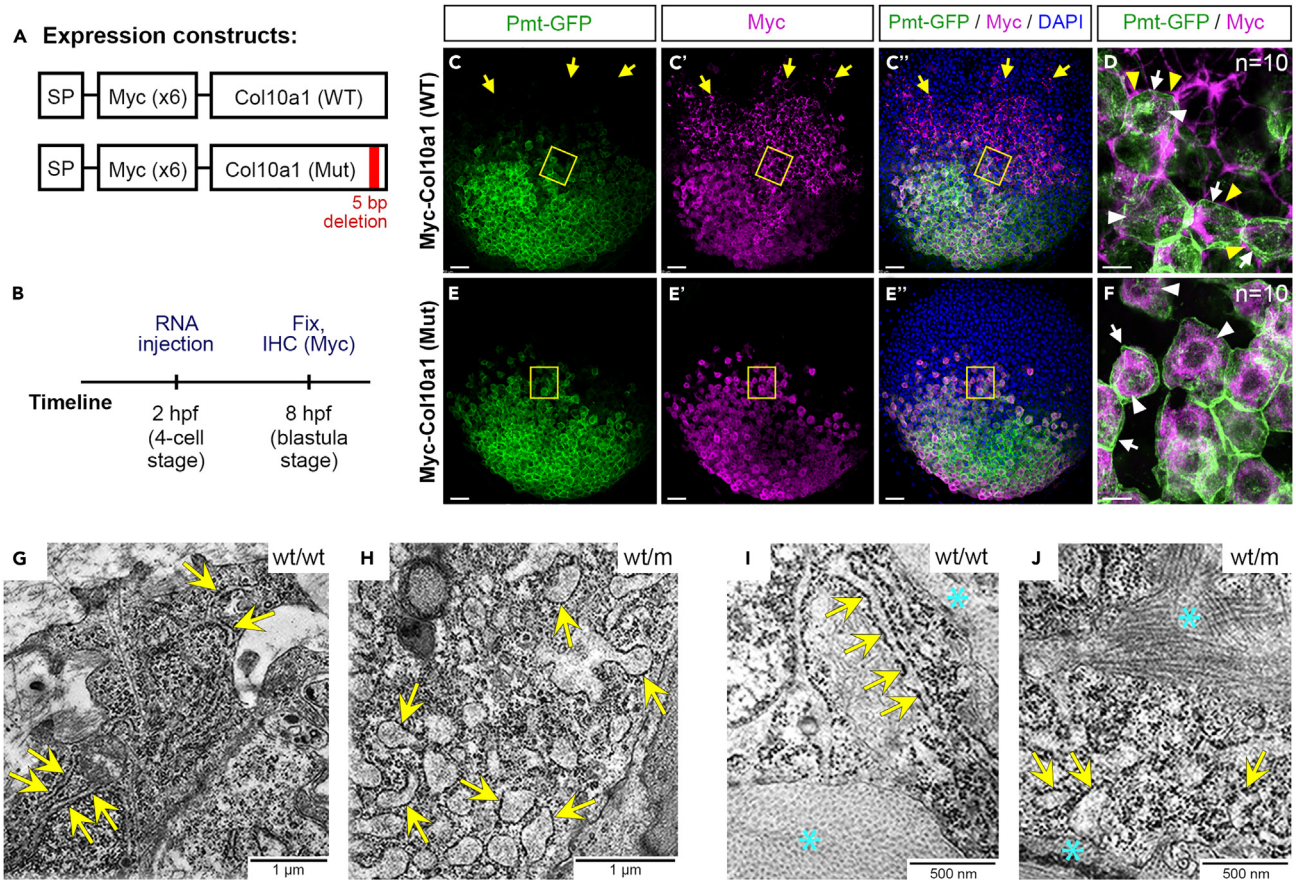

Figure 5. Mutant Col10a1$^{\Delta 633a}$ protein is intracellularly retained and mutant *col10a1*$^{\Delta 633a}$ cells have fragmented endoplasmic reticulum

(A–F) Overexpression and immunohistochemistry (IHC) of Myc-tagged medaka wild-type Col10a1 (WT) and mutant Col10a1$^{\Delta 633a}$ (Mut) in medaka embryos. Expression constructs and experimental timeline are shown in A and B, respectively. SP, signal peptide. Myc-tagged WT or mutant *col10a1* RNA was co-injected with *pmt-GFP* RNA into a single cell of four-cell stage medaka embryos at 2 h post fertilization (hpf). At 8 hpf, injected embryos were fixed for Myc IHC. Nuclei were stained with DAPI. Overview (C–C″, E–E″) and magnified (D, F; as indicated by yellow boxes in C–C″, E–E″, respectively) confocal images of stained 8 hpf medaka embryos. Images in (C)–(C″) and (E)–(E″) show 2D slices while (D) and (F) show 2.3 µm z stacks. Pmt-GFP signal marked cell boundaries (white arrows in D, F). Myc-tagged WT Col10a1 was detected intracellularly (white arrowheads, D), at cell-cell boundaries (yellow arrowheads, D), and in regions where Pmt-GFP signal was absent (yellow arrows, C–D). Myc-tagged mutant Col10a1 was detected only in intracellular regions (white arrowheads, F) in cells co-expressing Pmt-GFP (E–F). n = 10 embryos.

(G–J) TEM images showing the intracellular region of a chondrocyte in the pharyngeal cartilage in a WT/WT sibling (G) and WT/m mutant (H), as well as notochord transversal sections of a WT/WT sibling (I) and WT/m mutant (J) at 16 dpf. Yellow arrows mark ribosome-like structures on the endoplasmic reticulum (ER) cisternae. Compared to WT/WT, WT/m have swollen and fragmented RER. In addition, disorganized and reduced collagen fibers were observed in the WT/m mutant (I, cyan asterisks) compared to WT/WT sibling (J, cyan asterisks). Scale bars: (C–C″, E–E″) 50 µm, (D, F) 10 µm, (G, H) 1 µm, (I, J) 500 nm.

embryos (at 2 h post fertilization; hpf; Figures 5A and 5B). A *pmt-GFP* RNA was co-injected to visualize cell membranes.[40] Confocal imaging at 8 hpf revealed Pmt-GFP localization to cell membranes in approximately one-quarter of cells as expected (Figures 5C and 5E; n = 20 embryos). Control embryos injected with Myc-tagged WT *col10a1* mRNA had Myc signal in the intracellular space (Figure 5D; white arrowheads), at cell-cell boundaries (Figure 5D; yellow arrowheads), and extracellularly in regions where Pmt-GFP was not expressed indicating diffusion of Col10a1 in extracellular spaces (Figures 5C and 5D; yellow arrows; n = 10 out of 10 embryos analyzed). In contrast, all embryos injected with Myc-tagged mutant *col10a1*$^{\Delta 633a}$ mRNA had Myc signal exclusively localized intracellularly (Figure 5F; white arrowheads; n = 10 out of 10 embryos analyzed) and only in cells that co-expressed Pmt-GFP (Figures 5E and 5F; n = 10 out of 10 embryos analyzed). This suggests that any molecules with one or more Myc-tagged mutant *col10a1*$^{\Delta 633a}$ chains are unable to be secreted. In addition, these findings suggest that, in medaka embryos, mutant Col10a1$^{\Delta 633a}$ protein fails to be secreted and is retained intracellularly, similar to the situation in MCDS mouse and cell culture models.[15,17]

Next, to further validate *col10a1*$^{\Delta 633a}$ medaka as a suitable MCDS model, ER stress levels were assessed in *col10a1*-expressing cells. Previous studies had reported dilated ER cisternae and increased numbers of intracellular vesicles under ER-stress conditions.[41,42] Here, we used

CLEM of gill filament cartilage to assess ER morphology. This revealed a significant increase in the number of intracellular vesicles with a diameter ranging from 100 to 500 nm in WT/m chondrocytes (47.3 ± 16.1 intracellular vesicles, n = 201 cells, 3 fish) compared to WT/WT controls (19.3 ± 9.0 intracellular vesicles, n = 225 cells, 3 fish; Figure S9). Transmission electron microscopy (TEM) analysis of chondrocytes in pharyngeal cartilage (Figures 5G and 5H) as well as osteoblasts along the notochord (Figures 5I and 5J) at 16 dpf also showed increased numbers of intracellular vesicles in WT/m mutants. Closer examination of these vesicles in WT/m mutants showed ribosome-like structures, which were similar to ribosomes attached to the rough ER in WT/WT controls (yellow arrows in Figures 5G–5J). This suggests that the vesicles in WT/m mutants represent the rough ER, which was dilated and fragmented, in contrast to the rough ER in WT/WT controls, which appeared as long flattened sacs (Figures 5G–5J). In addition, we also noticed an irregular arrangement of collagen fibers in the osteoid around the notochord of WT/m mutants, compared to the tightly packed and regularly aligned fibers in WT/WT samples (cyan asterisks in Figures 5I and 5J). Together, TEM analysis provided morphological evidence for increased ER stress and impaired ECM organization in *col10a1* WT/m mutants.

Next, to examine transcriptomic changes that preceded structural irregularities in mutants, we isolated *col10a1*:nlGFP-expressing chondrocytes and osteoblast progenitors from WT/WT siblings and WT/m *col10a1*$^{\Delta 633a}$ medaka at 10 dpf by fluorescence-activated cell sorting (FACS) and performed RNA sequencing (RNA-seq). Compared to WT/WT siblings, 777 transcripts were found to be upregulated and 332 transcripts were found to be downregulated in WT/m mutants (Figure S10A). Also, while *col10a1* expression was lower in WT/m mutants compared to WT/WT siblings, there was no significant difference in expression levels of *col10a1b* in WT/m mutants and WT/WT siblings (Figure S10B). This suggested that *col10a1b* did not compensate for phenotypes observed in WT/m mutants. Gene ontology (GO) term and Kyoto Encyclopedia of Genes and Genomes (KEGG) pathway analyses revealed that a majority of genes significantly upregulated in mutants function in the ER and are involved in protein processing (Figure S11). Upregulation of three well-characterized ER stress markers, *activating transcription factor 3* (*atf3*),[43] *cysteine-rich with EGF-like domains 2* (*creld2*),[44] and *derlin-2* (*derl2*),[45] was validated by quantitative RT-PCR (RT-qPCR) using RNA extracted from whole 10 dpf WT/WT and WT/m embryos (Figure 6A; Table S1). In addition, RT-qPCR analysis at juvenile (18 dpf) and adult (5 mpf) stages showed upregulation in WT/m mutants of *bip*, encoding an ER chaperone that binds misfolded proteins,[46] and *chop*, encoding a pro-apoptotic transcription factor expressed in response to uncontrolled ER stress,[47] respectively (Figure S12). This suggests an accumulation of ER stress in WT/m mutants over time. RNA-seq and RT-qPCR also revealed downregulation of four secreted ECM components *hyaluronan and proteoglycan link protein 1b* (*hapln1b*), *collagen9a1a* (*col9a1a*), *cartilage intermediate layer protein* (*cilp*), and *periostin* (*postn*; Figure 6A; Table S1).

In addition, cytoskeleton modeling factors were found to be dysregulated in mutants (Figure 6A; Table S1). *Phosphatidylinositol-4,5-bisphospate 3-kinase catalytic subunit β* (*pik3cb*), encoding the catalytic subunit of phosphoinositide 3-kinases (PI3Ks), which are implicated in cytoskeleton modeling and cell polarity,[48] was upregulated in WT/m mutants. On the other hand, *refilin-A* (*rflna*), which facilitates actin bundling and branching,[49] *KN motif and ankyrin repeat domains 2* (*kank2*), which regulates actin polymerization[50] and links microtubules to integrins,[51] as well as *frizzled-10* (*fzd10*), which encodes a non-canonical Wnt/PCP receptor,[52] were downregulated in mutants (Figure 6A; Table S1).

Together, these expression changes suggest an elevation of ER stress in WT/m *col10a1* cells, which adapt by enhancing protein processing in the ER and reducing transcription of membrane and secreted proteins, possibly to lessen protein load in the ER and to restore ER homeostasis. In addition, transcriptional dysregulation of cytoskeleton modeling factors results in a disorganized cytoskeleton and disruption of cell polarity, leading to malformation of bone and cartilage structures.

ER stress and cell polarity defects in *col10a1*$^{\Delta 633a}$ WT/m mutants are rescued by CBZ

CBZ is a drug that promotes autophagy and proteosomal degradation pathways.[4,53] In HeLa cells transfected with mutant collagen type X constructs and ColX p.Asn617Lys mutant mice of an SV129/C57Bl6 mixed background, CBZ reduced ER stress caused by intracellular accumulation of mutant collagen type X and enhanced its intracellular degradation.[4] To test if CBZ can alleviate ER stress also in *col10a1*$^{\Delta 633a}$ WT/m medaka mutants, embryos were treated with 10 mg/L CBZ for 72 h from 6 to 9 dpf. At 10 dpf, RNA from CBZ-treated larvae was extracted and RT-qPCR was performed. In contrast to DMSO-treated larvae, no significant difference in gene expression was observed for ER stress markers *atf3*, *creld2*, and *derl2* when CBZ-treated WT/m mutants were compared to CBZ-treated WT/WT siblings (Figure 6A; Table S1). In addition, in contrast to DMSO-treated WT/m mutants where secreted ECM components such as *hapln1b*, *col9a1a*, *cilp*, and *postn* were downregulated as compared to DMSO-treated WT/WT siblings (Figure 6A; Table S1), there was no significant difference in gene expression of *hapln1b*, *col9a1a*, *cilp*, and *postn* in CBZ-treated WT/m mutants and CBZ-treated WT/WT siblings (Figure 6A; Table S1). This suggests undisrupted transcription of secreted proteins in CBZ-treated WT/m mutants. Furthermore, this indicates that accumulation of ER stress in WT/m mutants is suppressed upon CBZ treatment, similar to MCDS mouse and cell culture studies.[3,4]

Next, we examined whether early CBZ treatment was also able to rescue transcriptional dysregulation of cell polarity regulators *rflna*, *pik3cb*, *kank2*, and *fzd10* via RT-qPCR at 10 dpf (Figure 6A). In contrast to DMSO-treated WT/m mutants, in which *rflna*, *pik3cb*, *kank2*, and *fzd10* were significantly dysregulated as described earlier, expression of these genes in CBZ-treated WT/m mutants was rescued to levels seen in WT/WT siblings (Figure 6A; Table S1). This showed that early CBZ treatment prevented transcriptional dysregulation of cell polarity regulators in WT/m mutants. Finally, to test if CBZ treatment was also able to alleviate the structural distortions observed in WT/m mutants, larvae were subjected to three different CBZ doses (1, 10, or 20 mg/L) from 9 to 12 dpf and fixed at 13 dpf for Alcian blue staining. Structural distortion of ceratobranchials was quantified by tortuosity measurements (Figure 6B). For DMSO (control) and 1 mg/L CBZ treatments, WT/m ceratobranchials had a tortuosity that was significantly higher than that of WT/WT ceratobranchials (Figure 6C). In contrast, treatment with 10 mg/L and 20 mg/L CBZ significantly reduced structural tortuosity in WT/m mutants when compared to DMSO controls (Figures 6C and

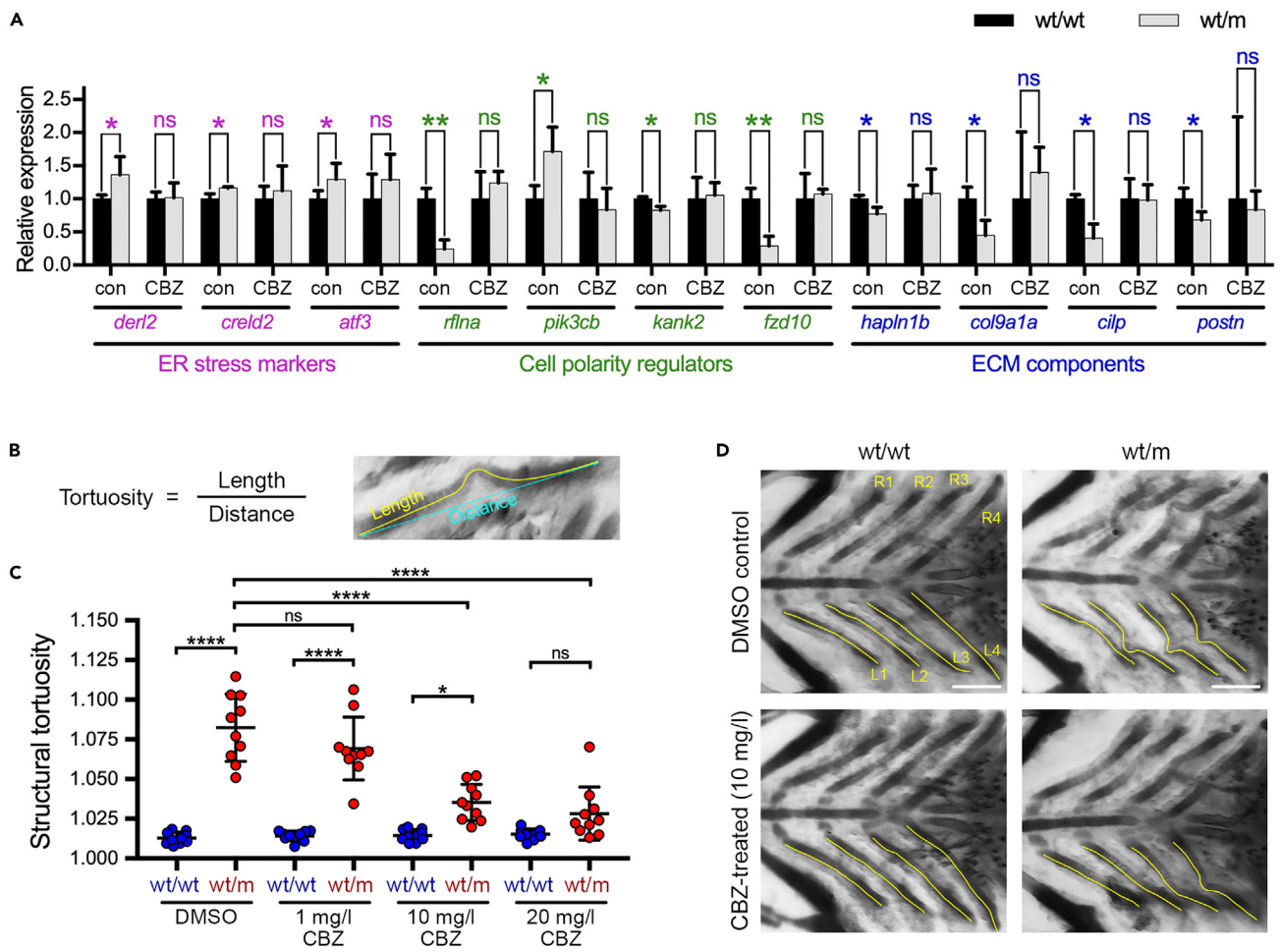

Figure 6. Carbamazepine alleviates cell polarity defects in *col10a1*$^{\Delta 633a}$ WT/m medaka mutants

(A) Expression analysis of ER stress markers *derl2*, *creld2*, and *atf3*, extracellular matrix (ECM) components *hapln1b*, *col9a1a*, *cilp*, and *postn*, as well as cytoskeleton regulators *rflna*, *pik3cb*, *kank2*, and *fzd10* in 10 dpf WT/WT siblings and WT/m mutants treated with DMSO (control; con) or carbamazepine (CBZ; 10 mg/L, from 6 dpf to 9 dpf). cDNA was purified from whole larvae. Error bars indicate mean ± s.d., *p < 0.05, **p < 0.01, ns, not significant, Student's two-tailed t test.

(B) Equation for measurement of tortuosity of ceratobranchials. Image shows an example of length and distance measurements of a 13 dpf mutant ceratobranchial.

(C) Comparison of ceratobranchial tortuosity in 13 dpf WtT/WT siblings and *col10a1*$^{\Delta 633}$ WT/m mutants treated with 1, 10, and 20 mg/L carbamazepine (CBZ) from 9 to 12 dpf. DMSO was used as control. Each data point indicates average tortuosity of eight ceratobranchials (R1-R4 and L1-L4 as shown in D) in one larva. n = 10 larvae. Error bars indicate mean ± s.d., *p < 0.05, ****p < 0.0001, ns, not significant, one-way ANOVA with Tukey's multiple comparisons test.

(D) Grayscale images of Alcian blue-stained ceratobranchials in WT/WT siblings and *col10a1*$^{\Delta 633a}$ WT/m mutants at 13 dpf. Larvae were treated with DMSO (control) or CBZ from 9 to 12 dpf. Yellow lines were manually drawn for measurement of tortuosity as shown in C. L1-L4, left ceratobranchials 1–4. R1-R4, right ceratobranchials 1–4. Scale bars: 100 μm.

6D). With 20 mg/L CBZ, no significant difference was observed in tortuosity of WT/WT and WT/m ceratobranchials (Figure 6C). Together, these findings implicate cell polarity defects as an immediate downstream effect of elevated ER stress in heterozygous *col10a1*$^{\Delta 633a}$ medaka mutants, highlighting a key role for cell polarity dysregulation in MCDS pathogenesis.

DISCUSSION

MCDS is a skeletal disorder caused by dominant mutations in the collagen type X trimerization domain.[1,2] Here, we showed that heterozygous *col10a1*$^{\Delta 633a}$ medaka carriers recapitulate typical features of human MCDS and identified impaired cell polarity as a potential cause for the observed skeletal defects. Importantly, both cell polarity impairments and skeletal defects were rescued by CBZ treatment. Thus, our findings establish the *col10a1*$^{\Delta 633}$ medaka mutant as a new animal model for MCDS that is suitable for MCDS drug screening.

Heterozygous *col10a1*$^{\Delta 633a}$ medaka mutants recapitulate MCDS

All *COL10A1* mutations associated with human MCDS are heterozygous.[20,54] In contrast to this, heterozygous *Col10a1* mutant mice displayed mild MCDS phenotypes, and only their homozygous siblings exhibited a disease severity that was similar to that in MCDS patients.[3,17] Here, we found that heterozygous *col10a1*$^{\Delta 633a}$ medaka recapitulated aspects of MCDS. On the other hand, survival of homozygous *col10a1*$^{\Delta 633a}$ medaka mutants declined drastically after approximately two weeks of age and no homozygous mutant survived beyond one month. Delayed osteoblast differentiation and disrupted bone formation may account for early lethality of m/m medaka mutants, but whether this is due to excessive ER stress or absence of functional collagen type X protein in the ECM remains to be determined.

Previous studies had shown that in MCDS defects in *COL10A1*-expressing hypertrophic chondrocytes led to impaired endochondral ossification, resulting in irregularly formed growth plates and short stature.[14,54] Although *Col10a1* expression differs considerably in mammals and teleost fish, with specific expression in hypertrophic chondrocytes in mammals but both chondrocytes and osteoblast progenitors in medaka and zebrafish,[6,28,29,55] the collagen type X trimerization domain is highly conserved.[20,56] Hence, we speculated that mutations in this domain in medaka may lead to similar cellular defects but different structural phenotypes when compared to MCDS. Other than in MCDS, where structural deformities occur in endochondral bones, we expected deformities in both bone and cartilage in *col10a1*$^{\Delta 633a}$ medaka mutants. In line with this, we showed that the ceratohyal bone, which in teleost fish develops via endochondral ossification,[57] was shorter in WT/m *col10a1*$^{\Delta 633a}$ medaka mutants. In addition, cartilaginous structures such as the ceratobranchials and gill filaments were severely deformed in the medaka mutants. In addition, WT/m *col10a1*$^{\Delta 633a}$ medaka mutants overall were also significantly shorter than their WT siblings. We observed aberrant and nondirectional bone matrix secretion from *col10a1*-expressing osteoblast progenitors positioned at the edges of vertebral centra. Thus, similar to MCDS in mammals, we found that the reduced body length in medaka mutants was likely due to shortened and hypermineralized vertebral bodies.

A key feature of MCDS is elevated ER stress in *COL10A1*-expressing cells.[16–18] In our study, we showed that, similar to MCDS mice,[18,19] genes involved in ER protein processing were significantly upregulated in WT/m *col10a1*$^{\Delta 633a}$ medaka mutants. In addition, genes encoding membrane and secreted proteins such as ECM structural proteins that are processed in the rough ER were downregulated. These changes in gene expression are characteristic for cells that are responding to elevated ER stress, i.e., to increase protein folding capacity and reduce protein load in the ER to alleviate stress,[58,59] and in line with transcriptome analyses in mice.[18,19] Consistently, closer examination of *col10a1*-expressing cells in WT/m mutants by electron microscopy revealed increased accumulation of intracellular vesicles as well as swollen and fragmented rough ER, another indicator of ER stress.[41] Together, this showed that WT/m *col10a1*$^{\Delta 633a}$ medaka mutants recapitulated important traits of MCDS.

Dysregulation of cell polarity results in MCDS-like skeletal deformities in medaka

MCDS is commonly characterized by deformities in cartilaginous growth plates.[18] Earlier studies had shown that the integrated stress response pathway contributes to chondrocyte differentiation defects in MCDS. This involves the protein kinase RNA-like ER kinase (PERK) signaling pathway, which activates ATF4 synthesis and subsequent ATF4-transactivation of *Sox9*, a transcription factor highly expressed in immature chondrocytes.[60] Other than this, however, it remains unclear how ER stress and chondrocyte differentiation defects lead to skeletal irregularities in MCDS. We observed an irregular arrangement of mutant *col10a1*-expressing chondrocytes in ceratobranchials and gill filaments in the medaka MCDS model, instead of the highly organized cell stacking seen in controls. Previous studies had shown that the regulation of chondrocyte polarity is important for columnar organization of chondrocytes in mice, chick, and zebrafish.[38,61–63] Hence, one possibility for the disorganized chondrocyte stacking observed in mutants was a disrupted cell polarity in *col10a1*-expressing chondrocytes. We confirmed this by γ-tubulin staining of MTOCs, which are indicators of chondrocyte polarity[38,64] and were positioned at opposing ends in *col10a1*$^{\Delta 633a}$ mutant chondrocytes. Also, nuclear division axes, which reflect the orientation of cell division and polarity,[62,65] displayed a reduction in division angle in *col10a1*$^{\Delta 633a}$ mutant chondrocytes, indicating impaired cell polarity.

Medaka is an acellular teleost; i.e., no osteoblasts or osteocytes get entrapped in bone matrix.[37,66,67] Instead, osteoblasts line the bone surface, are highly polarized, and deposit matrix with restricted directionality, preventing their entrapping within matrix.[68] In line with this, *col10a1*-expressing osteoblast progenitors in WT/WT controls were always positioned at the surface of mineralized bone and never embedded within matrix. In contrast, we observed that *col10a1*$^{\Delta 633a}$ mutant osteoblast progenitors were surrounded by mineralized matrix in the vertebral column. In addition, the Golgi apparatus was aberrantly positioned in mutant cells. This suggested an impairment of cell polarity also in mutant osteoblast progenitors, resulting in dysregulation of polarized matrix secretion and consequently irregular bone matrix formation.

Cell polarity is established and maintained by asymmetric distribution of intracellular proteins, organelles, or subcellular processes. It highly depends on the actin and microtubule cytoskeleton that facilitates organized organelle positioning, directs vesicular transport, and determines the orientation of cell division axes.[69,70] Hence, proteins controlling cytoskeletal modeling and remodeling are critical regulators of cell polarity. On the other hand, cell polarity is also influenced by extracellular cues from adjacent cells or the ECM, via activation of cell surface receptors that trigger intracellular signaling cascades.[71–73] Analysis of mutant *col10a1*:nlGFP medaka cells that were isolated by FACS at presymptomatic stages revealed a dysregulation of genes encoding cytoskeletal modulators and ECM components. Therefore, we concluded that cell polarity in *col10a1*$^{\Delta 633a}$ mutant osteoblast progenitors and chondrocytes was impaired both cell-autonomously by dysregulation of cytoskeletal regulators leading to a disorganized cytoskeletal network and non-cell-autonomously through disruption of the surrounding ECM. Whether these defects occur simultaneously or successively remains to be investigated. Consequently, however, mutant cells exhibited misaligned cell division axes and a loss of directional matrix secretion, which contributed to the deformation of skeletal structures.

Our findings are in line with earlier reports that elevated ER stress levels and the UPR influence cell polarity either directly via transcriptional modulation of cell polarity regulators or indirectly via modulation of factors influencing the cellular microenvironment. One example for a cell polarity regulator is MIST1, which is activated by the XBP1-dependent UPR pathway.[74] Likewise, ER stress has been reported to cause a reduction in the production of collagens,[75] which has been shown to disrupt cell polarity.[76,77] Taken together, our findings implicate the dysregulation of cell polarity because of increased ER stress and as an underlying mechanism contributing to MCDS pathogenesis.

Early CBZ treatment alleviates ER stress and rescues cell polarity defects in *col10a1*$^{\Delta 633a}$ medaka mutants

Currently, no drug has been approved for therapeutic use to treat MCDS. However, CBZ, approved for the treatment of epilepsy and nerve pain, is presently being repurposed and tested in a clinical trial for MCDS therapy. In MCDS mouse models and human cell cultures, CBZ relieved ER stress by stimulating intracellular proteolysis.[3,4] In addition, skeletal deformities in MCDS mice were rescued by CBZ treatment.[3,4] Here, we show that CBZ treatment in heterozygous *col10a1*$^{\Delta 633a}$ medaka mutants recapitulated these responses, including reduction of ER stress and rescuing skeletal deformities. Most importantly, however, we showed that early CBZ treatment also alleviated the dysregulation of cell polarity modulators in heterozygous *col10a1*$^{\Delta 633a}$ mutants. Previous studies had shown that CBZ functions as a sodium channel blocker[78] as well as enhances autophagy and proteolysis, thereby reducing ER stress.[3,4,53,79] However, so far, there are no reports on the influence of CBZ on cell polarity. Hence, we hypothesize that, in CBZ-treated *col10a1*$^{\Delta 633a}$ medaka mutants, dysregulation of cell polarity was attenuated via reduction of ER stress. Together, our data suggest that *col10a1*$^{\Delta 633a}$ medaka mutants are a suitable alternative platform for future MCDS drug screens *in vivo* in a model that offers short generation time, high fecundity, and the possibility to perform live imaging of bone cell behavior.

Limitations of the study

In this study, we used a medaka fish model to gain insights into molecular mechanisms underlying MCDS. Our finding that dysregulated polarity of *col10a1*-expressing cells coincides with skeletal irregularities in *col10a1*$^{\Delta 633a}$ medaka mutants opens the possibility that growth plate irregularities in MCDS patients are also caused by polarity loss in hypertrophic chondrocytes. However, evidently, there are marked differences in endochondral ossification in mammals and teleost fish.[80,81] Additional analysis is therefore warranted to uncover consequences of impaired cell polarity in mouse models and human patients. This will likely also reveal novel targets for future MCDS therapies.

STAR★METHODS

Detailed methods are provided in the online version of this paper and include the following:

- KEY RESOURCES TABLE
- RESOURCE AVAILABILITY
  - Lead contact
  - Material availability
  - Data and code availability
- EXPERIMENTAL MODEL AND STUDY PARTICIPANT DETAILS
  - Fish lines and maintenance
- METHOD DETAILS
  - Fluorescence-activated cell sorting and RNA sequencing
  - Quantitative PCR
  - Generation of expression constructs and RNA injections
  - Carbamazepine treatment
  - *In situ* hybridization and immunohistochemistry
  - Bone and cartilage staining
  - Confocal and stereo-microscope imaging
  - Correlative light-electron microscopy
  - Microtomography
- QUANTIFICATION AND STATISTICAL ANALYSIS

SUPPLEMENTAL INFORMATION

Supplemental information can be found online at https://doi.org/10.1016/j.isci.2024.109405.

ACKNOWLEDGMENTS

We acknowledge the Paul Scherrer Institut, Villigen, Switzerland, for provision of synchrotron radiation beamtime at the TOMCAT beamline X02DA of the SLS. We also thank the CBIS confocal unit and the DBS fish facility for continued support.

This project is supported by grants from the Singapore Ministry of Education (MOE2016-T2-2-086, MOE-T2EP30221-0008) and the National Research Foundation Singapore (NRF; NRF2017-NRF-ISF002-2671). W.H.T. received a President's Graduate Fellowship from the National University of Singapore and a Martin & Temminck Fellowship from Naturalis, Leiden.

AUTHOR CONTRIBUTIONS

W.H.T. and C.W. conceived the study and designed the experiments. W.H.T. performed the experiments and analyzed data. M.R., B.J.v.H., and F.M. contributed to microtomography experiments. D.L. assisted with TEM experiments. T.B.N. and P.M. assisted in CLEM experiments. W.H.T. and C.W. wrote the paper with assistance from all authors.

DECLARATION OF INTERESTS

The authors declare no competing interests.

Received: September 26, 2023
Revised: December 21, 2023
Accepted: February 29, 2024
Published: March 4, 2024

REFERENCES

1. Bateman, J.F., Wilson, R., Freddi, S., Lamandé, S.R., and Savarirayan, R. (2005). Mutations of COL10A1 in Schmid metaphyseal chondrodysplasia. Hum. Mutat. *25*, 525–534. https://doi.org/10.1002/humu.20183.
2. Mäkitie, O., Susic, M., Ward, L., Barclay, C., Glorieux, F.H., and Cole, W.G. (2005). Schmid type of metaphyseal chondrodysplasia and COL10A1 mutations–findings in 10 patients. Am. J. Med. Genet. *137a*, 241–248. https://doi.org/10.1002/ajmg.a.30855.
3. Forouhan, M., Sonntag, S., and Boot-Handford, R.P. (2018). Carbamazepine reduces disease severity in a mouse model of metaphyseal chondrodysplasia type Schmid caused by a premature stop codon (Y632X) in the Col10a1 gene. Hum. Mol. Genet. *27*, 3840–3853. https://doi.org/10.1093/hmg/ddy253.
4. Mullan, L.A., Mularczyk, E.J., Kung, L.H., Forouhan, M., Wragg, J.M., Goodacre, R., Bateman, J.F., Swanton, E., Briggs, M.D., and Boot-Handford, R.P. (2017). Increased intracellular proteolysis reduces disease severity in an ER stress-associated dwarfism. J. Clin. Invest. *127*, 3861–3865. https://doi.org/10.1172/jci93094.
5. Kielty, C.M., Kwan, A.P., Holmes, D.F., Schor, S.L., and Grant, M.E. (1985). Type X collagen, a product of hypertrophic chondrocytes. Biochem. J. *227*, 545–554. https://doi.org/10.1042/bj2270545.
6. Kong, R.Y., Kwan, K.M., Lau, E.T., Thomas, J.T., Boot-Handford, R.P., Grant, M.E., and Cheah, K.S. (1993). Intron-exon structure, alternative use of promoter and expression of the mouse collagen X gene, Col10a-1. Eur. J. Biochem. *213*, 99–111. https://doi.org/10.1111/j.1432-1033.1993.tb17739.x.
7. Tsang, K.Y., Tsang, S.W., Chan, D., and Cheah, K.S.E. (2014). The chondrocytic journey in endochondral bone growth and skeletal dysplasia. Birth Defects Res. C Embryo Today. *102*, 52–73. https://doi.org/10.1002/bdrc.21060.
8. Shen, G. (2005). The role of type X collagen in facilitating and regulating endochondral ossification of articular cartilage. Orthod. Craniofac. Res. *8*, 11–17. https://doi.org/10.1111/j.1601-6343.2004.00308.x.
9. Kwan, A.P., Cummings, C.E., Chapman, J.A., and Grant, M.E. (1991). Macromolecular organization of chicken type X collagen *in vitro*. J. Cell Biol. *114*, 597–604. https://doi.org/10.1083/jcb.114.3.597.
10. Chen, Q., Fitch, J.M., Linsenmayer, C., and Linsenmayer, T.F. (1992). Type X collagen: covalent crosslinking to hypertrophic cartilage-collagen fibrils. Bone Miner. *17*, 223–227. https://doi.org/10.1016/0169-6009(92)90741-u.
11. Rosati, R., Horan, G.S., Pinero, G.J., Garofalo, S., Keene, D.R., Horton, W.A., Vuorio, E., de Crombrugghe, B., and Behringer, R.R. (1994). Normal long bone growth and development in type X collagen-null mice. Nat. Genet. *8*, 129–135. https://doi.org/10.1038/ng1094-129.
12. Kwan, K.M., Pang, M.K., Zhou, S., Cowan, S.K., Kong, R.Y., Pfordte, T., Olsen, B.R., Sillence, D.O., Tam, P.P., and Cheah, K.S. (1997). Abnormal compartmentalization of cartilage matrix components in mice lacking collagen X: implications for function. J. Cell Biol. *136*, 459–471. https://doi.org/10.1083/jcb.136.2.459.
13. Bateman, J.F., Freddi, S., McNeil, R., Thompson, E., Hermanns, P., Savarirayan, R., and Lamandé, S.R. (2004). Identification of four novel COL10A1 missense mutations in schmid metaphyseal chondrodysplasia: further evidence that collagen X NC1 mutations impair trimer assembly. Hum. Mutat. *23*, 396. https://doi.org/10.1002/humu.9222.
14. Tsang, K.Y., Chan, D., Cheslett, D., Chan, W.C.W., So, C.L., Melhado, I.G., Chan, T.W.Y., Kwan, K.M., Hunziker, E.B., Yamada, Y., et al. (2007). Surviving endoplasmic reticulum stress is coupled to altered chondrocyte differentiation and function. PLoS Biol. *5*, e44. https://doi.org/10.1371/journal.pbio.0050044.
15. Wilson, R., Freddi, S., Chan, D., Cheah, K.S.E., and Bateman, J.F. (2005). Misfolding of collagen X chains harboring Schmid metaphyseal chondrodysplasia mutations results in aberrant disulfide bond formation, intracellular retention, and activation of the unfolded protein response. J. Biol. Chem. *280*, 15544–15552. https://doi.org/10.1074/jbc.M410758200.
16. Ho, M.S.P., Tsang, K.Y., Lo, R.L.K., Susic, M., Mäkitie, O., Chan, T.W.Y., Ng, V.C.W., Sillence, D.O., Boot-Handford, R.P., Gibson, G., et al. (2007). COL10A1 nonsense and frame-shift mutations have a gain-of-function effect on the growth plate in human and mouse metaphyseal chondrodysplasia type Schmid. Hum. Mol. Genet. *16*, 1201–1215. https://doi.org/10.1093/hmg/ddm067.
17. Rajpar, M.H., McDermott, B., Kung, L., Eardley, R., Knowles, L., Heeran, M., Thornton, D.J., Wilson, R., Bateman, J.F., Poulsom, R., et al. (2009). Targeted induction of endoplasmic reticulum stress induces cartilage pathology. PLoS Genet. *5*, e1000691. https://doi.org/10.1371/journal.pgen.1000691.
18. Cameron, T.L., Bell, K.M., Tatarczuch, L., Mackie, E.J., Rajpar, M.H., McDermott, B.T., Boot-Handford, R.P., and Bateman, J.F. (2011). Transcriptional profiling of chondrodysplasia growth plate cartilage reveals adaptive ER-stress networks that allow survival but disrupt hypertrophy. PLoS One *6*, e24600. https://doi.org/10.1371/journal.pone.0024600.
19. Wang, B., He, L., Miao, W., Wu, G., Jiang, H., Wu, Y., Qu, J., and Li, M. (2017). Identification of key genes associated with Schmid-type metaphyseal chondrodysplasia based on microarray data. Int. J. Mol. Med. *39*, 1428–1436. https://doi.org/10.3892/ijmm.2017.2954.
20. Zhang, C., Liu, J., Iqbal, F., Lu, Y., Mustafa, S., Bukhari, F., Lou, H., Fu, R., Wu, Z., Yang, X., et al. (2018). A missense point mutation in COL10A1 identified with whole-genome deep sequencing in a 7-generation Pakistan dwarf family. Heredity *120*, 83–89. https://doi.org/10.1038/s41437-017-0021-6.
21. Yu, T., Graf, M., Renn, J., Schartl, M., Larionova, D., Huysseune, A., Witten, P.E., and Winkler, C. (2017). A vertebrate-specific and essential role for osterix in osteogenesis revealed by gene knockout in the teleost medaka. Development *144*, 265–271. https://doi.org/10.1242/dev.139550.
22. Gistelinck, C., Kwon, R.Y., Malfait, F., Symoens, S., Harris, M.P., Henke, K., Hawkins, M.B., Fisher, S., Sips, P., Guillemyn, B., et al. (2018). Zebrafish type I collagen mutants faithfully recapitulate human type I

collagenopathies. Proc. Natl. Acad. Sci. USA *115*, E8037–E8046. https://doi.org/10.1073/pnas.1722200115.

23. Lawrence, E.A., Kague, E., Aggleton, J.A., Harniman, R.L., Roddy, K.A., and Hammond, C.L. (2018). The mechanical impact of col11a2 loss on joints; col11a2 mutant zebrafish show changes to joint development and function, which leads to early-onset osteoarthritis. Philos. Trans. R. Soc. Lond. B Biol. Sci. *373*, 20170335. https://doi.org/10.1098/rstb.2017.0335.
24. Hughes, A., Oxford, A.E., Tawara, K., Jorcyk, C.L., and Oxford, J.T. (2017). Endoplasmic Reticulum Stress and Unfolded Protein Response in Cartilage Pathophysiology; Contributing Factors to Apoptosis and Osteoarthritis. Int. J. Mol. Sci. *18*, 665. https://doi.org/10.3390/ijms18030665.
25. Ishikawa, T., Taniguchi, Y., Okada, T., Takeda, S., and Mori, K. (2011). Vertebrate unfolded protein response: mammalian signaling pathways are conserved in Medaka fish. Cell Struct. Funct. *36*, 247–259.
26. Lleras-Forero, L., Winkler, C., and Schulte-Merker, S. (2020). Zebrafish and medaka as models for biomedical research of bone diseases. Dev. Biol. *457*, 191–205. https://doi.org/10.1016/j.ydbio.2019.07.009.
27. Witten, P.E., Harris, M.P., Huysseune, A., and Winkler, C. (2017). Small teleost fish provide new insights into human skeletal diseases. Methods Cell Biol. *138*, 321–346. https://doi.org/10.1016/bs.mcb.2016.09.001.
28. Renn, J., Büttner, A., To, T.T., Chan, S.J.H., and Winkler, C. (2013). A col10a1:nlGFP transgenic line displays putative osteoblast precursors at the medaka notochordal sheath prior to mineralization. Dev. Biol. *381*, 134–143. https://doi.org/10.1016/j.ydbio.2013.05.030.
29. Renn, J., and Winkler, C. (2012). Osterix:nlGFP transgenic medaka identify regulatory roles for retinoic acid signaling during osteoblast differentiation *in vivo*. J. Appl. Ichthyol. *28*, 360–363. https://doi.org/10.1111/j.1439-0426.2012.01983.x.
30. Zhu, Y., Li, L., Zhou, L., Mei, H., Jin, K., Liu, K., Xu, W., Tang, J., Yang, Y., Zhao, R., and He, X. (2011). A novel mutation leading to elongation of the deduced alpha1(X) chain results in Metaphyseal Chondrodysplasia type Schmid. Clin. Chim. Acta *412*, 1266–1269. https://doi.org/10.1016/j.cca.2011.03.026.
31. Stratakis, C.A., Orban, Z., Burns, A.L., Vottero, A., Mitsiades, C.S., Marx, S.J., Abbassi, V., and Chrousos, G.P. (1996). Dideoxyfingerprinting (ddF) analysis of the type X collagen gene (COL10A1) and identification of a novel mutation (S671P) in a kindred with Schmid metaphyseal chondrodysplasia. Biochem. Mol. Med. *59*, 112–117. https://doi.org/10.1006/bmme.1996.0075.
32. Renn, J., and Winkler, C. (2009). Osterix-mCherry transgenic medaka for *in vivo* imaging of bone formation. Dev. Dynam. *238*, 241–248. https://doi.org/10.1002/dvdy.21836.
33. Harrison, G., Shapiro, I.M., and Golub, E.E. (1995). The phosphatidylinositol-glycolipid anchor on alkaline phosphatase facilitates mineralization initiation *in vitro*. J. Bone Miner. Res. *10*, 568–573. https://doi.org/10.1002/jbmr.5650100409.
34. Tan, W.H., and Winkler, C. (2022). A non-disruptive and efficient knock-in approach allows fate tracing of resident osteoblast progenitors during repair of vertebral lesions in medaka. Development *149*, dev200238. https://doi.org/10.1242/dev.200238.
35. Dasyani, M., Tan, W.H., Sundaram, S., Imangali, N., Centanin, L., Wittbrodt, J., and Winkler, C. (2019). Lineage tracing of col10a1 cells identifies distinct progenitor populations for osteoblasts and joint cells in the regenerating fin of medaka (Oryzias latipes). Dev. Biol. *455*, 85–99. https://doi.org/10.1016/j.ydbio.2019.07.012.
36. Ofer, L., Zaslansky, P., and Shahar, R. (2021). A comparison of the structure, composition and mechanical properties of anosteocytic vertebrae of medaka (O. latipes) and osteocytic vertebrae of zebrafish (D. rerio). J. Fish. Biol. *98*, 995–1006. https://doi.org/10.1111/jfb.14334.
37. Ofer, L., Dumont, M., Rack, A., Zaslansky, P., and Shahar, R. (2019). New insights into the process of osteogenesis of anosteocytic bone. Bone *125*, 61–73. https://doi.org/10.1016/j.bone.2019.05.013.
38. Le Pabic, P., Ng, C., and Schilling, T.F. (2014). Fat-Dachsous signaling coordinates cartilage differentiation and polarity during craniofacial development. PLoS Genet. *10*, e1004726. https://doi.org/10.1371/journal.pgen.1004726.
39. Stolper, J., Ambrosio, E.M., Danciu, D.P., Buono, L., Elliott, D.A., Naruse, K., Martínez-Morales, J.R., Marciniak-Czochra, A., and Centanin, L. (2019). Stem cell topography splits growth and homeostatic functions in the fish gill. Elife *8*, e43747. https://doi.org/10.7554/eLife.43747.
40. Liu, P., Sudhaharan, T., Koh, R.M.L., Hwang, L.C., Ahmed, S., Maruyama, I.N., and Wohland, T. (2007). Investigation of the dimerization of proteins from the epidermal growth factor receptor family by single wavelength fluorescence cross-correlation spectroscopy. Biophys. J. *93*, 684–698. https://doi.org/10.1529/biophysj.106.102087.
41. Kanemoto, S., Nitani, R., Murakami, T., Kaneko, M., Asada, R., Matsuhisa, K., Saito, A., and Imaizumi, K. (2016). Multivesicular body formation enhancement and exosome release during endoplasmic reticulum stress. Biochem. Biophys. Res. Commun. *480*, 166–172. https://doi.org/10.1016/j.bbrc.2016.10.019.
42. Rellmann, Y., and Dreier, R. (2018). Different Forms of ER Stress in Chondrocytes Result in Short Stature Disorders and Degenerative Cartilage Diseases: New Insights by Cartilage-Specific ERp57 Knockout Mice. Oxid. Med. Cell. Longev. *2018*, 8421394. https://doi.org/10.1155/2018/8421394.
43. Jiang, H.Y., Wek, S.A., McGrath, B.C., Lu, D., Hai, T., Harding, H.P., Wang, X., Ron, D., Cavener, D.R., and Wek, R.C. (2004). Activating transcription factor 3 is integral to the eukaryotic initiation factor 2 kinase stress response. Mol. Cell Biol. *24*, 1365–1377. https://doi.org/10.1128/MCB.24.3.1365-1377.2004.
44. Oh-hashi, K., Koga, H., Ikeda, S., Shimada, K., Hirata, Y., and Kiuchi, K. (2009). CRELD2 is a novel endoplasmic reticulum stress-inducible gene. Biochem. Biophys. Res. Commun. *387*, 504–510. https://doi.org/10.1016/j.bbrc.2009.07.047.
45. Oda, Y., Okada, T., Yoshida, H., Kaufman, R.J., Nagata, K., and Mori, K. (2006). Derlin-2 and Derlin-3 are regulated by the mammalian unfolded protein response and are required for ER-associated degradation. J. Cell Biol. *172*, 383–393. https://doi.org/10.1083/jcb.200507057.
46. Gething, M.J. (1999). Role and regulation of the ER chaperone BiP. Semin. Cell Dev. Biol. *10*, 465–472. https://doi.org/10.1006/scdb.1999.0318.
47. Nishitoh, H. (2012). CHOP is a multifunctional transcription factor in the ER stress response. J. Biochem. *151*, 217–219. https://doi.org/10.1093/jb/mvr143.
48. Shewan, A., Eastburn, D.J., and Mostov, K. (2011). Phosphoinositides in cell architecture. Cold Spring Harbor Perspect. Biol. *3*, a004796. https://doi.org/10.1101/cshperspect.a004796.
49. Gay, O., Gilquin, B., Assard, N., Stuelsatz, P., Delphin, C., Lachuer, J., Gidrol, X., and Baudier, J. (2016). Refilins are short-lived Actin-bundling proteins that regulate lamellipodium protrusion dynamics. Biol. Open *5*, 1351–1361. https://doi.org/10.1242/bio.019588.
50. Kakinuma, N., Zhu, Y., Wang, Y., Roy, B.C., and Kiyama, R. (2009). Kank proteins: structure, functions and diseases. Cell. Mol. Life Sci. *66*, 2651–2659. https://doi.org/10.1007/s00018-009-0038-y.
51. Paradžik, M., Humphries, J.D., Stojanović, N., Nestić, D., Majhen, D., Dekanić, A., Samaržija, I., Sedda, D., Weber, I., Humphries, M.J., and Ambriović-Ristov, A. (2020). KANK2 Links αVβ5 Focal Adhesions to Microtubules and Regulates Sensitivity to Microtubule Poisons and Cell Migration. Front. Cell Dev. Biol. *8*, 125. https://doi.org/10.3389/fcell.2020.00125.
52. Fukukawa, C., Nagayama, S., Tsunoda, T., Toguchida, J., Nakamura, Y., and Katagiri, T. (2009). Activation of the non-canonical Dvl-Rac1-JNK pathway by Frizzled homologue 10 in human synovial sarcoma. Oncogene *28*, 1110–1120. https://doi.org/10.1038/onc.2008.467.
53. Hidvegi, T., Ewing, M., Hale, P., Dippold, C., Beckett, C., Kemp, C., Maurice, N., Mukherjee, A., Goldbach, C., Watkins, S., et al. (2010). An autophagy-enhancing drug promotes degradation of mutant alpha1-antitrypsin Z and reduces hepatic fibrosis. Science *329*, 229–232. https://doi.org/10.1126/science.1190354.
54. Richmond, C.M., and Savarirayan, R. (2019). Schmid Metaphyseal Chondrodysplasia. In GeneReviews, M.P. Adam, H.H. Ardinger, R.A. Pagon, S.E. Wallace, L.J.H. Bean, K. Stephens, and A. Amemiya, eds.
55. Eames, B.F., Amores, A., Yan, Y.L., and Postlethwait, J.H. (2012). Evolution of the osteoblast: skeletogenesis in gar and zebrafish. BMC Evol. Biol. *12*, 27. https://doi.org/10.1186/1471-2148-12-27.
56. Hu, Y.L., Pan, X.M., Xiang, L.X., and Shao, J.Z. (2010). Characterization of C1q in teleosts: insight into the molecular and functional evolution of C1q family and classical pathway. J. Biol. Chem. *285*, 28777–28786. https://doi.org/10.1074/jbc.M110.131318.
57. Le Pabic, P., Dranow, D.B., Hoyle, D.J., and Schilling, T.F. (2022). Zebrafish endochondral growth zones as they relate to human bone size, shape and disease. Front. Endocrinol. *13*, 1060187. https://doi.org/10.3389/fendo.2022.1060187.
58. Almanza, A., Carlesso, A., Chintha, C., Creedican, S., Doultsinos, D., Leuzzi, B., Luís, A., McCarthy, N., Montibeller, L., More, S., et al. (2019). Endoplasmic reticulum stress signalling – from basic mechanisms to clinical

applications. FEBS J. *286*, 241–278. https://doi.org/10.1111/febs.14608.
59. Adams, C.J., Kopp, M.C., Larburu, N., Nowak, P.R., and Ali, M.M.U. (2019). Structure and Molecular Mechanism of ER Stress Signaling by the Unfolded Protein Response Signal Activator IRE1. Front. Mol. Biosci. *6*, 11. https://doi.org/10.3389/fmolb.2019.00011.
60. Wang, C., Tan, Z., Niu, B., Tsang, K.Y., Tai, A., Chan, W.C.W., Lo, R.L.K., Leung, K.K.H., Dung, N.W.F., Itoh, N., et al. (2018). Inhibiting the integrated stress response pathway prevents aberrant chondrocyte differentiation thereby alleviating chondrodysplasia. Elife *7*, e37673. https://doi.org/10.7554/eLife.37673.
61. Kuss, P., Kraft, K., Stumm, J., Ibrahim, D., Vallecillo-Garcia, P., Mundlos, S., and Stricker, S. (2014). Regulation of cell polarity in the cartilage growth plate and perichondrium of metacarpal elements by HOXD13 and WNT5A. Dev. Biol. *385*, 83–93. https://doi.org/10.1016/j.ydbio.2013.10.013.
62. Li, Y., Li, A., Junge, J., and Bronner, M. (2017). Planar cell polarity signaling coordinates oriented cell division and cell rearrangement in clonally expanding growth plate cartilage. Elife *6*, e23279. https://doi.org/10.7554/eLife.23279.
63. Sisson, B.E., Dale, R.M., Mui, S.R., Topczewska, J.M., and Topczewski, J. (2015). A role of glypican4 and wnt5b in chondrocyte stacking underlying craniofacial cartilage morphogenesis. Mech. Dev. *138*, 279–290. https://doi.org/10.1016/j.mod.2015.10.001.
64. Santos-Ledo, A., Garcia-Macia, M., Campbell, P.D., Gronska, M., and Marlow, F.L. (2017). Kinesin-1 promotes chondrocyte maintenance during skeletal morphogenesis. PLoS Genet. *13*, e1006918. https://doi.org/10.1371/journal.pgen.1006918.
65. Lu, M.S., and Johnston, C.A. (2013). Molecular pathways regulating mitotic spindle orientation in animal cells. Development *140*, 1843–1856. https://doi.org/10.1242/dev.087627.
66. Ekanayake, S., and Hall, B.K. (1987). The development of acellularity of the vertebral bone of the Japanese medaka, Oryzias latipes (Teleostei; Cyprinidontidae). J. Morphol. *193*, 253–261. https://doi.org/10.1002/jmor.1051930304.
67. Shahar, R., and Dean, M.N. (2013). The enigmas of bone without osteocytes. BoneKEy Rep. *2*, 343. https://doi.org/10.1038/bonekey.2013.77.
68. Ekanayake, S., and Hall, B.K. (1988). Ultrastructure of the osteogenesis of acellular vertebral bone in the Japanese medaka, Oryzias latipes (Teleostei, Cyprinidontidae). Am. J. Anat. *182*, 241–249. https://doi.org/10.1002/aja.1001820305.
69. Drubin, D.G., and Nelson, W.J. (1996). Origins of Cell Polarity. Cell *84*, 335–344. https://doi.org/10.1016/S0092-8674(00)81278-7.
70. Raman, R., Pinto, C.S., and Sonawane, M. (2018). Polarized Organization of the Cytoskeleton: Regulation by Cell Polarity Proteins. J. Mol. Biol. *430*, 3565–3584. https://doi.org/10.1016/j.jmb.2018.06.028.
71. Berzat, A., and Hall, A. (2010). Cellular responses to extracellular guidance cues. EMBO J. *29*, 2734–2745. https://doi.org/10.1038/emboj.2010.170.
72. Yonemura, S. (2014). Differential Sensitivity of Epithelial Cells to Extracellular Matrix in Polarity Establishment. PLoS One *9*, e112922. https://doi.org/10.1371/journal.pone.0112922.
73. Théry, M., Racine, V., Piel, M., Pépin, A., Dimitrov, A., Chen, Y., Sibarita, J.-B., and Bornens, M. (2006). Anisotropy of cell adhesive microenvironment governs cell internal organization and orientation of polarity. Proc. Natl. Acad. Sci. USA *103*, 19771–19776. https://doi.org/10.1073/pnas.0609267103.
74. Hess, D.A., Strelau, K.M., Karki, A., Jiang, M., Azevedo-Pouly, A.C., Lee, A.H., Deering, T.G., Hoang, C.Q., MacDonald, R.J., and Konieczny, S.F. (2016). MIST1 Links Secretion and Stress as both Target and Regulator of the Unfolded Protein Response. Mol. Cell Biol. *36*, 2931–2944. https://doi.org/10.1128/mcb.00366-16.
75. Vonk, L.A., Doulabi, B.Z., Huang, C.L., Helder, M.N., Everts, V., and Bank, R.A. (2010). Endoplasmic reticulum stress inhibits collagen synthesis independent of collagen-modifying enzymes in different chondrocyte populations and dermal fibroblasts. Biochem. Cell. Biol. *88*, 539–552. https://doi.org/10.1139/o09-174.
76. Izu, Y., Sun, M., Zwolanek, D., Veit, G., Williams, V., Cha, B., Jepsen, K.J., Koch, M., and Birk, D.E. (2011). Type XII collagen regulates osteoblast polarity and communication during bone formation. J. Cell Biol. *193*, 1115–1130. https://doi.org/10.1083/jcb.201010010.
77. Watanabe, M., Kosumi, H., Osada, S.I., Takashima, S., Wang, Y., Nishie, W., Oikawa, T., Hirose, T., Shimizu, H., and Natsuga, K. (2021). Type XVII collagen interacts with the aPKC-PAR complex and maintains epidermal cell polarity. Exp. Dermatol. *30*, 62–67. https://doi.org/10.1111/exd.14196.
78. Kennebäck, G., Bergfeldt, L., and Tomson, T. (1995). Electrophysiological evaluation of the sodium-channel blocker carbamazepine in healthy human subjects. Cardiovasc. Drugs Ther. *9*, 709–714. https://doi.org/10.1007/bf00878554.
79. Meng, Q., Chen, X., Sun, L., Zhao, C., Sui, G., and Cai, L. (2011). Carbamazepine promotes Her-2 protein degradation in breast cancer cells by modulating HDAC6 activity and acetylation of Hsp90. Mol. Cell. Biochem. *348*, 165–171. https://doi.org/10.1007/s11010-010-0651-y.
80. Witten, P.E., and Huysseune, A. (2009). A comparative view on mechanisms and functions of skeletal remodelling in teleost fish, with special emphasis on osteoclasts and their function. Biol. Rev. Camb. Phil. Soc. *84*, 315–346. https://doi.org/10.1111/j.1469-185X.2009.00077.x.
81. Giovannone, D., Paul, S., Schindler, S., Arata, C., Farmer, D.T., Patel, P., Smeeton, J., and Crump, J.G. (2019). Programmed conversion of hypertrophic chondrocytes into osteoblasts and marrow adipocytes within zebrafish bones. Elife *8*, e42736. https://doi.org/10.7554/eLife.42736.
82. Stemmer, M., Thumberger, T., Del Sol Keyer, M., Wittbrodt, J., and Mateo, J.L. (2015). CCTop: An Intuitive, Flexible and Reliable CRISPR/Cas9 Target Prediction Tool. PLoS One *10*, e0124633. https://doi.org/10.1371/journal.pone.0124633.
83. Buettner, A., Sundaram, S., Vyas, H., Yu, T., Mathavan, S., and Winkler, C. (2018). Fluorescence-activated cell sorting (FACS) of osteoblasts and osteoclasts for RNA sequencing in a medaka, Oryzias latipes (Temming & Schlegel, 1846), osteoporosis model. J. Appl. Ichthyol. *34*, 481–488. https://doi.org/10.1111/jai.13660.
84. Liu, R., Imangali, N., Ethiraj, L.P., Carney, T.J., and Winkler, C. (2022). Transcriptome Profiling of Osteoblasts in a Medaka (Oryzias latipes) Osteoporosis Model Identifies Mmp13b as Crucial for Osteoclast Activation. Front. Cell Dev. Biol. *10*, 775512. https://doi.org/10.3389/fcell.2022.775512.
85. Raudvere, U., Kolberg, L., Kuzmin, I., Arak, T., Adler, P., Peterson, H., and Vilo, J. (2019). g:Profiler: a web server for functional enrichment analysis and conversions of gene lists (2019 update). Nucleic Acids Res. *47*, W191–W198. https://doi.org/10.1093/nar/gkz369.
86. Luo, W.G., Liu, H.Z., Lin, W.H., Kabir, M.H., and Su, Y. (2013). Simultaneous splicing of multiple DNA fragments in one PCR reaction. Biol. Proced. Online *15*, 9. https://doi.org/10.1186/1480-9222-15-9.
87. Wagner, T.U., Renn, J., Riemensperger, T., Volff, J.N., Köster, R.W., Goerlich, R., Schartl, M., and Winkler, C. (2003). The teleost fish medaka (Oryzias latipes) as genetic model to study gravity dependent bone homeostasis *in vivo*. Adv. Space Res. *32*, 1459–1465. https://doi.org/10.1016/s0273-1177(03)90381-4.
88. Renn, J., and Winkler, C. (2010). Characterization of collagen type 10a1 and osteocalcin in early and mature osteoblasts during skeleton formation in medaka. J. Appl. Ichthyol. *26*, 196–201. https://doi.org/10.1111/j.1439-0426.2010.01404.x.
89. Glinka, M., Herrmann, T., Funk, N., Havlicek, S., Rossoll, W., Winkler, C., and Sendtner, M. (2010). The heterogeneous nuclear ribonucleoprotein-R is necessary for axonal beta-actin mRNA translocation in spinal motor neurons. Hum. Mol. Genet. *19*, 1951–1966. https://doi.org/10.1093/hmg/ddq073.
90. Yu, T., Witten, P.E., Huysseune, A., Buettner, A., To, T.T., and Winkler, C. (2016). Live imaging of osteoclast inhibition by bisphosphonates in a medaka osteoporosis model. Dis. Model. Mech. *9*, 155–163. https://doi.org/10.1242/dmm.019091.
91. Walker, M.B., and Kimmel, C.B. (2007). A two-color acid-free cartilage and bone stain for zebrafish larvae. Biotech. Histochem. *82*, 23–28. https://doi.org/10.1080/10520290701333558.
92. Liu, Y., Tran, B.N., Wang, F., Ounjai, P., Wu, J., and Hew, C.L. (2016). Visualization of Assembly Intermediates and Budding Vacuoles of Singapore Grouper Iridovirus in Grouper Embryonic Cells. Sci. Rep. *6*, 18696. https://doi.org/10.1038/srep18696.
93. Kukulski, W., Schorb, M., Welsch, S., Picco, A., Kaksonen, M., and Briggs, J.A.G. (2012). Precise, correlated fluorescence microscopy and electron tomography of lowicryl sections using fluorescent fiducial markers. Methods Cell Biol. *111*, 235–257. https://doi.org/10.1016/b978-0-12-416026-2.00013-3.

STAR★METHODS

KEY RESOURCES TABLE

REAGENT or RESOURCE	SOURCE	IDENTIFIER
Antibodies		
Mouse anti-c-Myc	DSHB	Cat# 9E10; RRID: AB_2266850
Mouse anti-GM130	BD Biosciences	Cat# 610822; RRID: AB_398141
Rabbit anti-gamma-tubulin	GeneTex	Cat# GTX113286; RRID: AB_10725043
Goat anti-mouse Alexa Fluor 568	Abcam	Cat# ab175473; RRID: AB_2895153
Goat anti-mouse Alexa Fluor 633	Invitrogen	Cat# A-21052; RRID: AB_2535719
Goat anti-rabbit Alexa Fluor 633	Invitrogen	Cat# A-21070; RRID: AB_2535731
Biological samples		
Medaka embryonic, larval and adult tissue samples	This paper	N/A
Chemicals, peptides, and recombinant proteins		
Carbamazepine	Sigma	Cat# C4024
Trypsin	HyClone	Cat# SH30042.01
Collagenase	Sigma	Cat# C2674
Calcein	Sigma	Cat# C0875
Alizarin Complexone	Sigma	Cat# A3882
Cas9 nuclease	Integrated DNA Technologies	Cat# 1081059
Critical commercial assays		
Direct-zol RNA MicroPrep kit	Zymo Research	Cat# R2060
RevertAid First Strand cDNA Synthesis Kit	ThermoFisher Scientific	Cat# K1621
mMESSAGE mMACHINE SP6 kit	Invitrogen	Cat# AM1340
Deposited data		
Raw and analyzed RNAseq data from purified *col10a1* cells of *col10a1*$^{\Delta 633a}$ medaka mutants and wildtype siblings	This paper	GEO: GSE233581
Experimental models: Organisms/strains		
Medaka: *Tg(col10a1:nlGFP)*	Renn et al., 2013	N/A
Medaka: *Tg(osx:mCherry)*	Renn & Winkler, 2009	N/A
Medaka: *col10a1*$^{\Delta 633a}$ mutant	This paper	N/A
Oligonucleotides		
CRISPR/Cas9 guide RNA for generating *col10a1*$^{\Delta 633a}$ mutant: 5′-CCACTGCACTTTCTCTGGGTTCC-3′	This paper	N/A
Forward primer for genotyping *col10a1*$^{\Delta 633a}$ mutant: 5′-GGCAGCCCCATTAAGTTCGACC-3′	This paper	N/A
Reverse primer for genotyping *col10a1*$^{\Delta 633a}$ mutant: 5′-TGTCTCCGTTACAAAAGGTCACCG-3′	This paper	N/A
RT-qPCR primers	Table S1, this paper	N/A
Primers for generating pCS2-myc-col10wt and pCS2-myc-col10mut expression constructs	Table S1, this paper	N/A
Recombinant DNA		
Plasmid: pCS2-myc-col10wt	This paper	N/A
Plasmid: pCS2-myc-col10mut	This paper	N/A

(*Continued on next page*)

Continued

REAGENT or RESOURCE	SOURCE	IDENTIFIER
Software and algorithms		
Fiji ImageJ	Stemmer et al.[82]	https://fiji.sc/
Prism 7	GraphPad	https://www.graphpad.com/
ExPASy	Swiss Institute of Bioinformatics	https://www.expasy.org/resources/translate
Clustal Omega Multiple Sequence Alignment	European Molecular Biology Laboratory	https://www.ebi.ac.uk/Tools/msa/clustalo/#:~:text=Clustal%20Omega%20is%20a%20new,our%20pairwise%20sequence%20alignment%20tools.
g:Profiler	Buettner et al.[83]	https://biit.cs.ut.ee/gprofiler/gost
Bio-Rad CFX Maestro	Bio-Rad	https://www.bio-rad.com/de-de/sku/12013758-cfx-maestro-software-2-3-for-windows-pc?ID=12013758
Imaris	Oxford Instruments	https://imaris.oxinst.com/
Adobe Photoshop CC	Adobe	https://www.adobe.com/products/photoshop.html

RESOURCE AVAILABILITY

Lead contact

Further information and requests for resources and reagents should be directed to and will be fulfilled by the lead contact, Christoph Winkler (dbswcw@nus.edu.sg).

Material availability

Plasmids and medaka lines generated in this study are available upon request to the lead contact, Christoph Winkler (dbswcw@nus.edu.sg).

Data and code availability

- The RNAseq data have been deposited in the NCBI GEO database and is publicly available under the accession number GEO: GSE233581. Microscopy data reported in this study will be shared by the lead contact upon request.
- No original code was used in this study.
- Any additional information required to reanalyze the data reported in this paper is available from the lead contact upon request.

EXPERIMENTAL MODEL AND STUDY PARTICIPANT DETAILS

Fish lines and maintenance

All medaka lines were maintained and handled according to protocols approved by the Institutional Animal Care and Use Committee (IACUC) of the National University of Singapore (NUS; protocol numbers: R18-0562, BR19-0120). 2 hpf, 8 hpf, 10 dpf, 12 dpf, 16 dpf, 18 dpf, 28 dpf, 3 mpf and 5 mpf medaka were used for experiments. Sex of medaka was not considered as a variable in this study. Transgenic *col10a1*:nlGFP and *osx*:mCherry lines were previously described.[28,32] The nlGFP in *col10a1*:nlGFP is leaky and hence, GFP is detected in both nucleus and cytoplasm. For generation of the *col10a1*$^{\Delta 633a}$ medaka mutant, a CRISPR/Cas9 guide RNA (gRNA; 5'-CCACTGCACTTTCT CTGGGTTCC-3') was designed using CCTop[82] and generated by Integrated DNA Technologies (IDT; Singapore) as crRNA. 36 ng/µl of crRNA was co-injected with tracrRNA (67 ng/µl, IDT #1072533) and Cas9 nuclease (0.25 µg/µl, IDT #1081059) into the cytoplasm of one-cell stage medaka embryos. Injected fish were genotyped by Polymerase Chain Reaction-Restriction Fragment Length Polymorphism (PCR-RFLP) using the primer pair 5'-GGCAGCCCCATTAAGTTCGACC-3' and 5'-TGTCTCCGTTACAAAAGGTCAC CG-3', and the restriction enzyme *BtsI* (NEB #R0667). Amino acid sequence prediction and alignment were performed using ExPASy (Swiss Institute of Bioinformatics; SIB) and Clustal Omega Multiple Sequence Alignment (European Molecular Biology Laboratory; EMBL), respectively.

METHOD DETAILS

Fluorescence-activated cell sorting and RNA sequencing

To isolate *col10a1*:nlGFP cells, fluorescence-activated cell sorting (FACS) was performed as described previously[83] with slight modifications. Briefly, thirty 10 dpf *col10a1*:nlGFP-expressing larvae were chosen by random selection and dissociated in 0.23 % trypsin (HyClone SH30042.01) and 1.8 mg/ml collagenase (Sigma C2674), followed by FACS using a BD FACSAria II cytometer (BD Biosciences). RNAs from FACS-isolated cells were purified using the Direct-zol RNA MicroPrep kit (Zymo Research R2060) following manufacturer's instructions. RNA sequencing and bioinformatics analysis were performed by Novogene (Singapore) and as described previously.[84] GO term and KEGG pathway analyses were performed on differentially expressed genes identified with a threshold of $p<0.05$, using g:Profiler (version

e109_eg56_p17_1d3191d) with g:SCS multiple testing correction method applying a significance threshold of 0.05.[85] Blinding was not performed. RNA sequencing data are available in the NCBI Gene Expression Omnibus (GEO) database under the accession number GSE233581.

Quantitative PCR

For expression analysis by quantitative PCR, the Bio-Rad CFX96 Touch Real-Time PCR Detection System and PowerUp SYBR Green Master Mix (Applied Biosystems A25742) were used. RNA from whole larvae at 10 dpf (20 larvae per biological replicate; larvae chosen by random selection) and 18 dpf (7 larvae per biological replicate; larvae chosen by random selection), as well as gills dissected at 5 mpf (one gill per biological replicate; fish chosen by random selection), were extracted using TRIzol (Invitrogen 15596-018) and reverse-transcribed using a RevertAid First Strand cDNA Synthesis Kit (ThermoFisher Scientific K1621). β-actin was used for normalization. Primers used are listed in Table S2. All experiments were performed with at least three biological replicates and three technical replicates per biological replicate. Data analysis was performed using the Bio-Rad CFX Maestro software version 4.1.2434.232. Blinding was not performed. An unpaired Student's t-test was used for determination of statistical significance.

Generation of expression constructs and RNA injections

To generate pCS2-myc-col10wt and pCS2-myc-col10mut expression constructs, WT and mutant *col10a1* coding sequences were PCR amplified from cDNA isolated from WT medaka and the *col10a1*$^{\Delta 633a}$ medaka mutant, respectively. By overlap extension PCR ([86]; primers listed in Table S3), a Myc tag (sequence in Table S3; generated as a gBlock by IDT) was inserted in-frame and downstream of the signal peptide sequence in both WT and mutant *col10a1* coding sequences. Myc-tagged *col10a1* sequences were then ligated to a pCS2+ vector downstream of an SP6 promoter via *EcoRI* (NEB R0101S) and *XbaI* (NEB R0145S) restriction sites. To generate capped mRNAs, expression constructs were linearized by *XbaI* and *in vitro* transcribed using the mMESSAGE mMACHINE SP6 kit (Invitrogen AM1340). 200 ng/μl of WT or mutant *col10a1* RNA was co-injected with 20 ng/μl of *pmt-gfp* RNA (kindly provided by Thorsten Wohland, National University of Singapore;[40]) into a single cell of four-cell stage medaka embryos at 2 hpf. Injected embryos were fixed at 8 hpf for immunohistochemistry.

Carbamazepine treatment

Carbamazepine (Sigma C4024) was dissolved in 100 % DMSO to obtain stock concentrations of 1 mg/ml, 10 mg/ml and 20 mg/ml. Stock solutions were stored at 4°C in the dark. To obtain working solutions with carbamazepine concentrations at 1 mg/l, 10 mg/l and 20 mg/l, the 1 mg/ml, 10 mg/ml and 20 mg/ml stock solutions were diluted 1000x using fish medium, respectively. For drug treatment, larvae were immersed in carbamazepine working solution and kept in a 28°C incubator. Treatment with 0.1 % DMSO in fish medium was performed as control.

In situ hybridization and immunohistochemistry

Whole-mount RNA *in situ* hybridization was performed as described.[32] *runx2*,[87] *col10a1*,[88] and *osx*[32] riboprobes were generated as described previously. Immunohistochemistry was carried out on whole embryos and cryosections according to[89] and,[35] respectively. For immunohistochemistry on whole embryos, specimens were first fixed in 4% paraformaldehyde (PFA)/1x PBS at 4°C overnight. Next, specimens were washed with 1x PBST thrice (5 mins per wash at RT) and dechorionated manually using forceps. For immunohistochemistry on cryosections, glass slides containing cryosections stored at -20°C were thawed at RT for an hour, followed by rehydration of cryosections with 1x PBST for 5 mins in a glass coplin jar. For blocking, both whole embryos and cryosections were incubated in 1x PBDT (0.5 % Triton X-100, 0.5 % Tween-20, 2.5 % sheep serum, 1 % bovine serum albumin, 1 % DMSO, 1x PBS) for two hours at RT. After blocking, whole embryos and cryosections were incubated in primary antibody solution at 4°C overnight. Primary antibodies used are as follows: mouse anti-c-Myc (1:100, DSHB 9E10), mouse anti-GM130 (1:150, BD Biosciences 610822), rabbit anti-γ-Tubulin (1:200, GeneTex GTX113286). Next, whole embryos and cryosections were washed with 1x PBST 5 times (5 mins per wash) and incubated in secondary antibody solution for two hours at RT. Secondary antibodies used are as follows: goat anti-mouse Alexa Fluor 568 (1:500, Abcam ab175473), goat anti-mouse Alexa Fluor 633 (1:500, Invitrogen A-21052) and goat anti-rabbit Alexa Fluor 633 (1:500, Invitrogen A-21070). Finally, stained specimens were washed with 1x PBST 5 times (5 mins per wash), counterstained with DAPI (0.25 μg/ml; incubation for 10 mins at RT) and mounted in Mowiol 4-88 (Calbiochem) for imaging.

Bone and cartilage staining

In vivo staining of mineralized bone matrix in medaka larvae was performed as described in.[90] Medaka larvae were incubated in the dark at RT for two hours with either Calcein solution (0.01 % in fish medium; Sigma C0875) or Alizarin Complexone solution (ALC; 0.1 % in fish medium; Sigma A3882). Stained larvae were then washed with fish medium thrice at RT (15 mins per wash) and mounted in 1.2 % low melting agarose on a glass bottom petri fish for fluorescence imaging. Staining of bone and cartilage in fixed medaka specimens was carried out according to.[91] Specimens were first fixed in 4 % PFA/1x PBS for at least 2 hours at RT or overnight at 4°C. Fixed specimens were then washed with 1x PBST thrice (10 mins per wash) on a rotator at RT. For fixed larvae bone staining, larvae were incubated in a staining solution containing 0.5 % KOH and 0.05 % Alizarin Red S (Sigma A5533) for 2 hours in the dark at RT. For fixed larvae cartilage staining, larvae were incubated in a staining solution containing 70 % ethanol, 0.1 M $MgCl_2$ and 0.02 % Alcian Blue (Sigma A3157) overnight in the dark at RT. For fixed adult bone staining, adult medaka specimens were incubated in a staining solution containing 1 % KOH and 1 mg/ml Alizarin Red S overnight in the dark at RT. For fixed adult cartilage staining, adult medaka specimens were incubated in a staining solution containing 20 % acetic acid, 80 % ethanol and

0.15 mg/ml Alcian Blue overnight in the dark at RT. Stained specimens were washed in a series of 1 % KOH solutions with increasing glycerol concentrations (25 %, 50 % and 75 %; 1 hour per solution) and incubated in 100 % glycerol for imaging.

Confocal and stereo-microscope imaging

For live imaging, larvae were anaesthetized with 0.016% Tricaine (Sigma MS-222) and mounted in 1.2% low melting agarose on a glass bottom petri dish. Imaging was performed using the Olympus FluoView FV3000 confocal microscope, Zeiss LSM800 confocal microscope and Nikon SMZ18 stereomicroscope equipped with the NIS-Elements BR 3.0 software. Images were processed using ImageJ, Bitplane Imaris and Adobe Photoshop CC 2018.

Correlative light-electron microscopy

For analysis of intracellular features in *col10a1*-expressing cells, gills of 3 mpf medaka were dissected and cryo-fixed by High Pressure Freezing (HPF) Compact 01 system as described previously,[92] with modifications. Briefly, dissected gills were mounted in 1.2% low melting agarose, then placed on hexacidine-coated aluminum carriers and frozen by HPF. Cryo-fixed samples were next freeze-substituted using Leica EM AFS2, and embedded in Lowricryl HM20 resin as described in.[93] Briefly, freeze substitution was performed at –90°C for 48 to 58 hours using 0.1 % uranyl acetate in glass distilled acetone. Samples were then washed with acetone thrice at –45°C and incubated in increasing concentrations of Lowricryl HM20 (10 %, 25 %, 50 %, 75 %; 4 hours per incubation) in acetone while temperature was raised to –25°C. UV polymerization was then performed for 48 hours. Next, samples were sectioned at 70 nm thickness or otherwise stated with a Leica EM UC6 ultramicrotome. Sections were first examined using an Olympus FluoView FV3000 confocal microscope for identification of *col10a1*:nlGFP-expressing cells, and then imaged by a FEI Tecnai 120 keV transmission electron microscope (TEM) equipped with a 4k x 4k CCD Ultrascan camera (Gatan). Confocal images were processed by Bitplane Imaris while TEM images were collected with Gatan DigitalMicrograph.

Microtomography

For microfocus- and synchrotron-based X-ray tomographic microscopy, medaka specimens were fixed in 4% paraformaldehyde (Sigma), 1% glutaraldehyde (Sigma), 0.02 M sodium dihydrogen phosphate monohydrate ($NaH_2PO_4.H_2O$; Merck) and 0.08 M sodium phosphate dibasic heptahydrate ($Na_2HPO_4.7H_2O$; Merck) at room temperature overnight. Fixed specimens were stored in 70% ethanol and whole specimens were imaged using the Zeiss Xradia 520 Versa 3D X-ray microscope at Naturalis Biodiversity Center, Leiden, The Netherlands. Specimens were mounted in agarose and scanned at 40kV over 180° with 801 to 1601 projections. Exposure times ranging from 8 to 13 s resulted in a voxel size of 4.82 to 48.18 μm. Synchrotron radiation X-ray tomographic microscopy (SRXTM) was used for regions of interest of critical point dried specimens at the TOMCAT beamline, Swiss Light Source (SLS), Paul Scherrer Institut (PSI), Villigen, Switzerland. Acquisition of scans with 1501 projections over 180° using a 10x objective resulted in a voxel size of 0.65 μm. Energy settings ranging from 12 to 15 keV with exposure timings of 220 to 350 ms were used. Volume renderings and images of tomographic slides were processed using the Avizo 9.5.0 software.

QUANTIFICATION AND STATISTICAL ANALYSIS

The number of biological replicates and description of statistical tests performed are available in the associated figure legend of the experiment as well as in the main text of the paper. For RNA sequencing, three biological replicates were used for WT and two biological replicates were used for mutants. For all RT-qPCR experiments, three biological replicates were used for both WT and mutants. For analysis of ceratobranchial tortuosity, 10 biological replicates were used for both WT and mutants. Statistical analysis was performed using either GraphPad Prism 7.0a or Bio-Rad CFX Maestro version 4.1.2434.232. For comparison between two groups, an unpaired Student's t-test was used. For comparison of three groups or more, the one-way ANOVA with Tukey's multiple comparisons test was used. Significance levels are as indicated: * $p<0.05$; ** $p<0.01$; *** $p<0.001$; **** $p<0.0001$. All data are presented as mean ± s.d.